

AD-A092 724

MASSACHUSETTS INST OF TECH LEXINGTON LINCOLN LAB  
SOLID STATE RESEARCH, 1980:2.(U)  
MAY 80 A L MCWHORTER

F/6 20/12

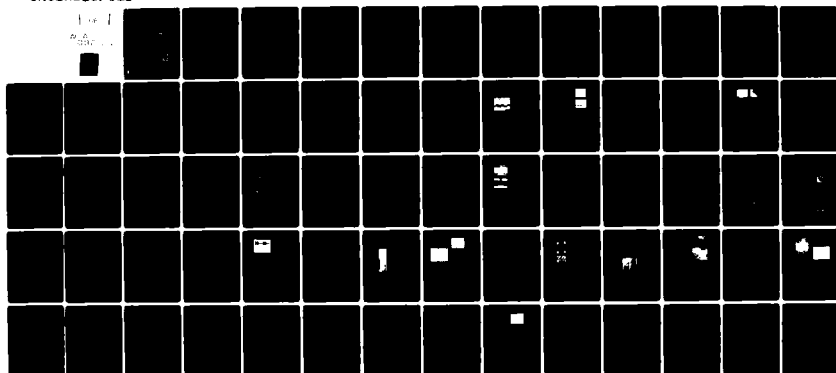
F19628-80-C-0002

UNCLASSIFIED

ESD-TR-80-36

NL

1 of 1  
P.A.  
500



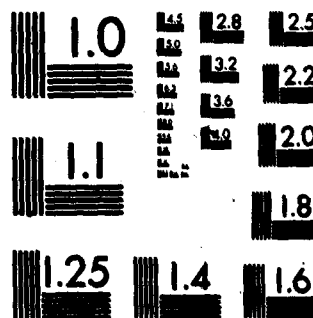
END

DATE

FILED

1-8

DTIC



MICROCOPY RESOLUTION TEST CHART  
NATIONAL BUREAU OF STANDARDS-1963-A

AD A092724

2

# Solid State Research

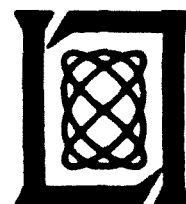
1980

Prepared  
under Electronic Systems Division Contract F19628-80-C-0002 by

## Lincoln Laboratory

MASSACHUSETTS INSTITUTE OF TECHNOLOGY

LEXINGTON, MASSACHUSETTS



Approved for public release; distribution unlimited.

The work reported in this document was performed at Lincoln Laboratory, a center for research operated by Massachusetts Institute of Technology, with the support of the Department of the Air Force under Contract F19628-80-C-0002.

This report may be reproduced to satisfy needs of U.S. Government agencies.

The views and conclusions contained in this document are those of the contractor and should not be interpreted as necessarily representing the official policies, either expressed or implied, of the United States Government.

This technical report has been reviewed and is approved for publication.

FOR THE COMMANDER

*Raymond L. Loiselie*

Raymond L. Loiselie, Lt. Col., USAF  
Chief, ESD Lincoln Laboratory Project Office

Non-Lincoln Recipients

**PLEASE DO NOT RETURN**

Permission is given to destroy this document  
when it is no longer needed.

MASSACHUSETTS INSTITUTE OF TECHNOLOGY  
LINCOLN LABORATORY

SOLID STATE RESEARCH

QUARTERLY TECHNICAL SUMMARY REPORT

1 FEBRUARY - 30 APRIL 1980

ISSUED 23 SEPTEMBER 1980

Approved for public release; distribution unlimited.

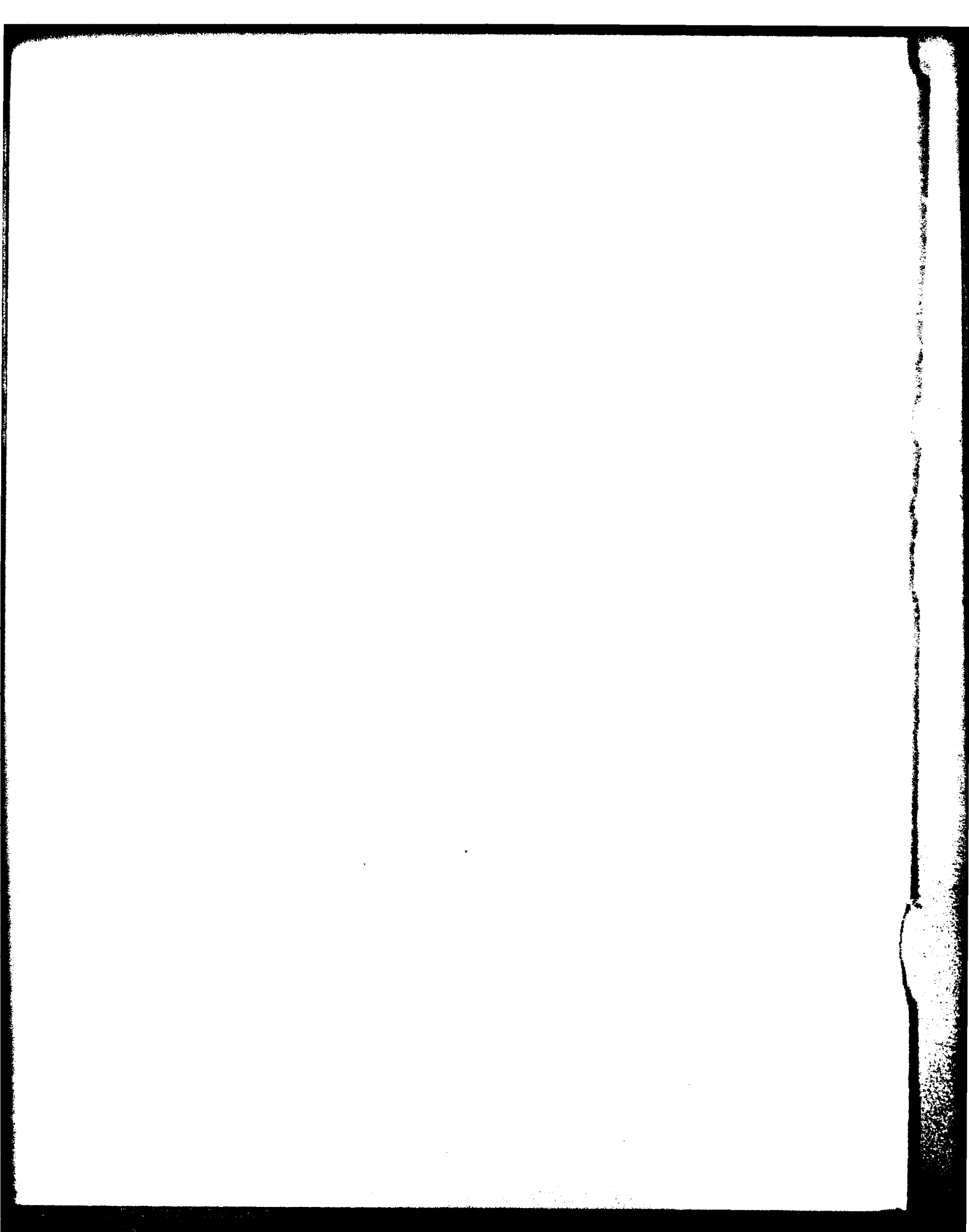
LEXINGTON

MASSACHUSETTS

# ABSTRACT

This report covers in detail the solid state research work of the Solid State Division at Lincoln Laboratory for the period 1 February through 30 April 1980. The topics covered are Solid State Device Research, Quantum Electronics, Materials Research, Microelectronics and Analog Device Technology. Funding is primarily provided by the Air Force, with additional support provided by the Army, DARPA, Navy, NASA, NSF, and DOE.

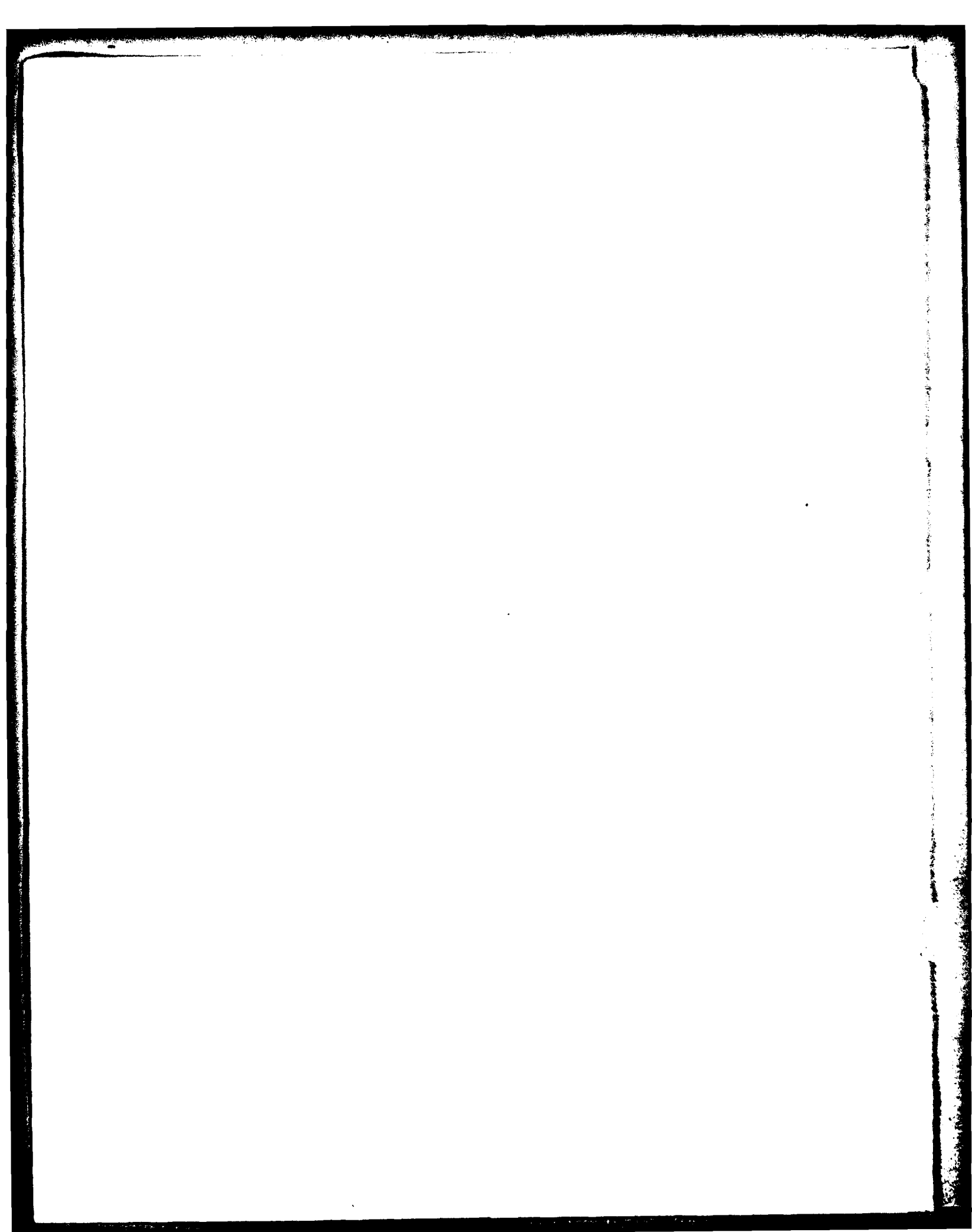
Accession For	
NTIS GRA&I	<input checked="" type="checkbox"/>
DDC TAB	<input type="checkbox"/>
Unannounced	<input type="checkbox"/>
Justification	
By	
Distribution/	
Availability Codes	
Dist.	Avail and/or special
A	



## CONTENTS

Abstract	iii
Introduction	vii
Reports on Solid State Research	xi
Organization	xviii
 I. SOLID STATE DEVICE RESEARCH	 1
A. High-Speed Operation of LiNbO <sub>3</sub> Electrooptic Interferometric Waveguide Modulators	1
B. Thickness of LPE Ga <sub>x</sub> In <sub>1-x</sub> As <sub>y</sub> P <sub>1-y</sub> Layers Nearly Lattice-Matched to (100) InP Substrates	3
C. LPE Surface Morphology of InP(Zn)	5
D. Liquidus Measurements in the Te-Corner of the Hg-Cd-Te Phase Diagram	6
 II. QUANTUM ELECTRONICS	 11
A. Laser Remote Sensing of C <sub>2</sub> H <sub>4</sub>	11
B. Optically Pumped Ce:LaF <sub>3</sub> Laser at 286 nm	13
C. One-Step Repair of Transparent Defects in Hard-Surface Photolithographic Masks via Laser Photodeposition	15
D. Solar Cell Fabrication by Laser Photochemical Doping	17
 III. MATERIALS RESEARCH	 19
The Cleft Process, a Technique for Producing Epitaxial Films on Reusable Substrates	19
 IV. MICROELECTRONICS	 25
A. Charge-Coupled Devices: SAW/MOSFET Memory Correlator	25
B. Charge-Coupled Devices: Programmable Matched Filter	26
C. X-Ray Lithography at ~100 Å Linewidths Using X-Ray Masks Fabricated by Shadowing Techniques	29
D. Submicrometer-Gate-Length GaAs FET	33
 V. ANALOG DEVICE TECHNOLOGY	 37
A. Application of a SAW Chirp Spectrum Analyzer to an Infrared Doppler Radar	37
1. Introduction	37
2. Infrared Radar	37
3. Signal Processing Trade-offs	39
4. Processor Implementation	41
B. Two-Port Impulsing of RACs for High-Accuracy SAW Transform Systems	43
C. Design Criteria for Surface-Acoustic-Wave Convolvers	44
1. Introduction	44
2. LTI Filter Representation for Propagation Effects	45
3. Design Criteria	46





## INTRODUCTION

### I. SOLID STATE DEVICE RESEARCH

High-speed operation of  $\text{LiNbO}_3$  electrooptic interferometric waveguide modulators for use in optical A/D converters has been demonstrated. Modulation up to 1.4 GHz has been achieved and RF modulation of the 275-MHz pulse train from a CW mode-locked frequency-doubled Nd:YAG laser has been observed.

A systematic study of the LPE growth of  $\text{Ga}_x\text{In}_{1-x}\text{As}_y\text{P}_{1-y}$  has been carried out over the entire range of layer compositions which are nearly lattice-matched to InP substrates. The results of the investigation enable the LPE-grown layer thickness to be calculated for various values of step-cooling, growth time, and composition.

A terraced surface morphology is found to be characteristic of heavily Zn-doped InP layers grown by LPE on substrates nominally oriented to (100). Noticeably smoother growth results if the substrates are oriented to a critical angle, which other workers have determined to be  $2.6^\circ$  off (100) in a  $\langle 110 \rangle$  direction. For not intentionally doped and Sn-doped growths, the terraced morphology is not evident and use of substrates oriented to the critical angle or those accurately oriented to (100) does not improve the morphology.

Liquidus measurements have been carried out in the Te-corner of the Hg-Cd-Te phase diagram by a modified direct observational method. The technique eliminates supercooling as a source of error and yields liquidus temperatures significantly higher than previous values for solution compositions of interest for the liquid phase epitaxial growth of  $\text{Hg}_{1-x}\text{Cd}_x\text{Te}$  from Te-rich melts.

### II. QUANTUM ELECTRONICS

Remote-sensing measurements of  $\text{C}_2\text{H}_4$  have been made at ranges up to 2.7 km with a  $\text{CO}_2$  laser differential-absorption LIDAR system, which has been significantly improved by the incorporation of a dual-computer high-speed digital data acquisition system. In addition, preliminary statistical analysis of the LIDAR returns has been used to study the effect of atmospheric turbulence.

Ultraviolet laser action has been obtained from a 5d-4f transition in  $\text{Ce}^{3+}$ -doped  $\text{LaF}_3$ . The 286-nm wavelength obtained is the shortest of any solid-state laser.

A technique for simple, one-step correction of transparent defects in hard-surface, photolithographic masks has been demonstrated. The correction process uses laser photodeposition of a metal film from a metal-alkyl parent gas.

A pulsed ArF excimer laser has been used to fabricate silicon solar cells. The laser causes localized photolysis of  $\text{Al}(\text{CH}_3)_3$  or  $\text{B}(\text{CH}_3)_3$ , which combined with laser heating, produces p-doped regions on n-Si substrates.

### III. MATERIALS RESEARCH

By using a new technique, the CLEFT process, multiple single-crystal GaAs films have been grown by vapor-phase epitaxy on reusable substrates and transferred without significant degradation to secondary glass substrates. Because it can greatly reduce the quantity of bulk single-crystal material needed in the fabrication of semiconductor devices utilizing thin active regions, the CLEFT process should permit a drastic reduction in the cost of devices such as solar cells where wafer cost is currently a major factor; because it can be used to obtain high-quality single-crystal films on a variety of secondary substrates, the process can provide new approaches to the fabrication of integrated circuits on insulating substrates and of multilayer devices and circuits.

### IV. MICROELECTRONICS

A SAW/MOSFET gap-coupled memory correlator which uses an array of MOSFETs to record an image of a SAW reference waveform from sampling fingers on a silicon chip has been demonstrated. The reference waveform is entered at the input of a SAW device, and a subsequent SAW signal is multiplied by the sampled reference and the products summed on an output electrode.

A 32-stage CCD transversal filter with taps programmable as 6-bit digital words has been built using a new architecture which allows more stages and more bits per tap to be achieved in a given chip area than was possible with earlier designs. The key to this design is the use of a multiplying D/A converter at the inputs to the filter. Matched filtering using a chirp waveform has been demonstrated with this device.

A new technique for fabricating high-contrast X-ray masks with precisely controlled linewidths smaller than  $100 \text{ \AA}$  has been developed. The technique is based on the deposition at an oblique angle of X-ray absorber material onto relief structures of triangular and square section in a polyimide membrane.

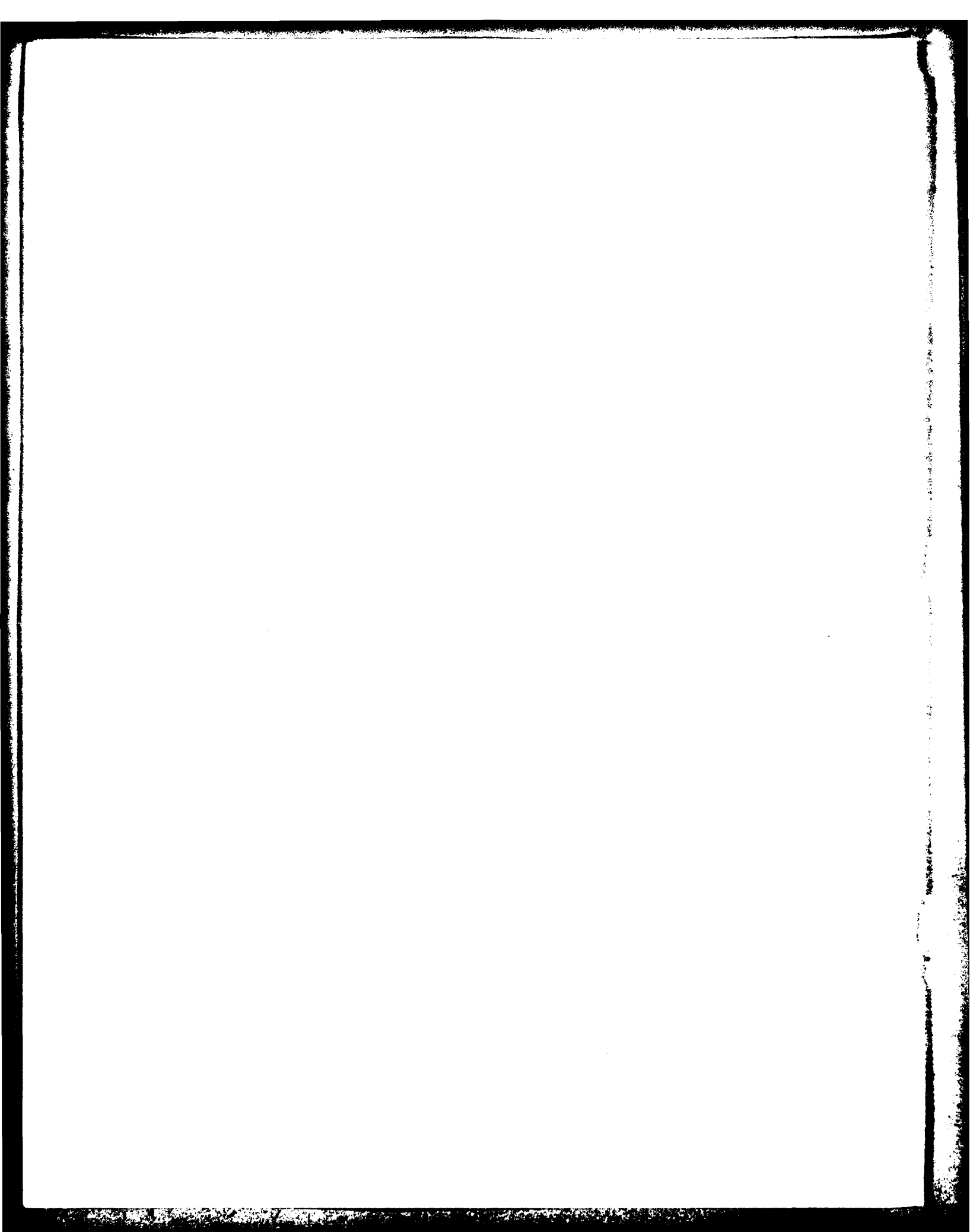
A submicrometer gate-length GaAs FET has been fabricated as a test vehicle for the development of a device processing sequence which would not require alignment when writing or replicating the submicrometer patterns. Submicrometer alignment is eliminated by having the gate-processing step precede the ohmic contact step. A typical device with total gate dimensions of  $0.45 \text{ }\mu\text{m}$  by  $104 \text{ }\mu\text{m}$  exhibits a noise figure of 3.5 dB at 12 GHz, with an associated gain of 5 dB.

### V. ANALOG DEVICE TECHNOLOGY

A surface-acoustic-wave (SAW) spectrum analyzer has been incorporated as the key signal-processing element in a prototype infrared airborne radar. The processor is designed to identify signals from moving targets while rejecting noise and ground clutter returns in order to provide automatic target acquisition. An analysis of the signal-processing trade-offs for various processors shows that the SAW equipment developed is well matched to the infrared radar application.

A novel method of maintaining accuracy in a chirp-Fourier-transform system has been demonstrated in which each port of the reflective-array expander device is sequentially impulsed. Use of this new technique permits controlled shifts in digitally timed impulses to generate the precise chirp waveforms required, and thereby greatly simplifies the task of automatically preserving system stability.

The effects of acoustic dispersion and attenuation on the performance of SAW convolvers are shown to be equivalent to an ideal SAW convolver in cascade with a linear time-invariant filter. Using this result, the implementation loss due to acoustic dispersion and attenuation, transducer band-pass response, and input/output matching networks has been calculated. Design criteria include the effects of phase and amplitude distortion which are representative of typical convolvers.



# REPORTS ON SOLID STATE RESEARCH

15 February through 15 May 1980

## PUBLISHED REPORTS

### Journal Articles

<u>JA No.</u>			
5001	Effects of Narrow-Free-Spectral-Range Etalons of Mode-Locked Lasers	S. R. Chinn	<i>Opt. Commun.</i> <u>31</u> , 359 (1979)
5014	Solid-Phase Growth of Large Aligned Grains During Scanned Laser Crystallization of Amorphous Ge Films on Fused Silica	J. C. C. Fan H. J. Zeiger R. P. Gale R. L. Chapman	<i>Appl. Phys. Lett.</i> <u>36</u> , 158 (1980)
5017	Shallow-Homojunction GaAs Cells with High Resistance to 1-MeV Electron Radiation	J. C. C. Fan R. L. Chapman C. O. Bozler P. J. Drevinsky*	<i>Appl. Phys. Lett.</i> <u>36</u> , 53 (1980)
5022	Metal-Atom Resonance-Line Lasers	D. J. Ehrlich R. M. Osgood, Jr.	<i>IEEE J. Quantum Electron.</i> <u>QE-16</u> , 257 (1980)
5027	Development of a High-Repetition-Rate Mini-TEA CO <sub>2</sub> Laser	N. Menyuk P. F. Moulton	<i>Rev. Sci. Instrum.</i> <u>51</u> , 216 (1980)
5038	Self-Sustained Pulsations in GainAsP Diode Lasers	J. N. Walpole T. A. Lind J. J. Hsieh A. G. Foyt	<i>Appl. Phys. Lett.</i> <u>36</u> , 240 (1980)
5048	Nonvolatile Analog Memory in MNOS Capacitors	R. S. Withers R. W. Ralston E. Stern	<i>IEEE Electron Devices Lett.</i> <u>EDL-1</u> , 42 (1980)
5050	Remote Sensing of CO Using Frequency-Doubled CO <sub>2</sub> Laser Radiation	D. K. Killinger N. Menyuk W. E. DeFeo	<i>Appl. Phys. Lett.</i> <u>36</u> , 402 (1980)
5057	Observation of Stimulated Level Shifting in Inverted Atomic Thallium Populations	D. J. Ehrlich R. M. Osgood, Jr. A. Sanchez	<i>Phys. Rev. Lett.</i> <u>44</u> , 871 (1980)
5060	Laser-Induced Microscopic Etching of GaAs and InP	D. J. Ehrlich R. M. Osgood, Jr. T. F. Deutsch	<i>Appl. Phys. Lett.</i> <u>36</u> , 698 (1980)
5102	Ohmic Contacts to Silicon Devices Formed by Ion Implantation and Laser Annealing	D. J. Silversmith R. W. Mountain S. C. Munroe M. W. Geis	<i>Solid State Technol.</i> <u>23</u> , 88 (1980)

\* Author not at Lincoln Laboratory.

# Meeting Speeches

## MS No.

- |       |  |  |  |
|-------|--|--|--|
| 4960A | Development and Applications of High-Speed InP Optoelectronic Switches   | F. J. Leonberger<br>P. F. Moulton                                | Topical Meeting on Integrated and Guided-Wave Optics, Incline Village, Nevada, 28-30 January 1980, Technical Digest, pp. WC5-1-WC5-4                                     |
| 5049  | Wideband LiNbO <sub>3</sub> Elastic Convolver with Parabolic Horns   | R. A. Becker<br>D. H. Hurlburt                                   | <u>1979 Ultrasonics Symposium Proceedings</u> (IEEE, New York, 1979), pp. 729-731  |
| 5058  | Effects of Temperature-Dependent Anisotropy in RAC Devices and a Cut of Quartz for a Temperature-Compensated RAC | D. E. Oates<br>R. C. Williamson                                  | <u>1979 Ultrasonics Symposium Proceedings</u> (IEEE, New York, 1979), pp. 691-695  |
| 5059  | Four-Wave Interactions in Acoustoelectric Integrating Correlators  | R. W. Ralston<br>E. Stern  | <u>1979 Ultrasonics Symposium Proceedings</u> (IEEE, New York, 1979), pp. 761-766  |
| 5060  | A SAW Accumulating Correlator with CCD Readout   | R. W. Ralston<br>D. L. Smythe<br>E. Stern                        | <u>1979 Ultrasonics Symposium Proceedings</u> (IEEE, New York, 1979), pp. 771-775  |
| 5061  | A CCD-Programmable SAW Matched Filter  | D. L. Smythe<br>R. W. Ralston<br>E. Stern                        | <u>1979 Ultrasonics Symposium Proceedings</u> (IEEE, New York, 1979), pp. 767-770  |
| 5062  | Wide Bandwidth Acoustoelectric Convolver   | I. Yao<br>S. A. Reible   | <u>1979 Ultrasonics Symposium Proceedings</u> (IEEE, New York, 1979), pp. 701-705  |
| 5081  | Integrated Surface Acoustic Wave/Charge-Coupled Device (SAW/CCD) Signal Processing Devices                       | D. L. Smythe<br>R. W. Ralston                                    | Proc. SPIE Vol. 209: <u>Optical Signal Processing for C<sup>3</sup>I</u> (Society of Photo-Optical Instrumentation Engineers, Bellingham, Washington, 1980), pp. 152-158 |
| 5082  | A Satellite-Borne SAW Chirp-Transform System for Uplink Demodulation of FSK Communication Signals                | R. C. Williamson<br>V. S. Dolat<br>R. R. Rhodes<br>D. M. Boroson | <u>1979 Ultrasonics Symposium Proceedings</u> (IEEE, New York, 1979), pp. 741-747  |
| 5106  | Comparison of Acoustoelectric and Acousto-optic Signal Processing Devices  | R. A. Becker<br>S. A. Reible<br>R. W. Ralston                    | Proc. SPIE Vol. 209: <u>Optical Signal Processing for C<sup>3</sup>I</u> (Society of Photo-Optical Instrumentation Engineers, Bellingham, Washington, 1980), pp. 126-133 |
| 5133A | Laser Photochemical Techniques for Semiconductor Processing  | T. F. Deutsch<br>D. J. Ehrlich<br>R. M. Osgood, Jr.              | Conf. on Laser and Electro-optical Systems, OSA/IEEE, San Diego, California, 26-28 February 1980, Digest of Technical Papers, p. 108                                     |

MS No.

- |      |   |   |   |
|------|---|---|---|
| 5167 | Device Requirements for Spread-Spectrum Communication                 | J. H. Cafarella                             | Proc. SPIE Vol. 209: <u>Optical Signal Processing for C<sup>3</sup>I</u> (Society of Photo-Optical Instrumentation Engineers, Bellingham, Washington, 1980), pp. 53-56      |
| 5183 | Advances in Transition-Metal-Doped Solid-State Lasers                 | P. F. Moulton<br>A. Mooradian               | Conf. on Laser and Electro-optical Systems, OSA/IEEE, San Diego, California, 26-28 February 1980, Digest of Technical Papers, p. 102  |
| 5186 | Remote Sensing of NO Using a Differential Absorption LIDAR            | N. Menyuk<br>D. K. Killinger<br>W. E. DeFeo | Conf. on Laser and Electro-optical Systems, OSA/IEEE, San Diego, California, 26-28 February 1980, Digest of Technical Papers, p. 94   |
| 5219 | High-Speed Electro-Optical Signal Conversion Devices                  | F. J. Leonberger                            | Proc. SPIE Vol. 218: <u>Devices and Systems for Optical Signal Processing</u> (Society of Photo-Optical Instrumentation Engineers, Bellingham, Washington, 1980), pp. 41-46 |
| 5248 | Acoustoelectric Microcircuits: A New Technology for Signal Processing | R. W. Ralston                               | <u>1980 IEEE International Symposium on Circuits and Systems Proceedings</u> (IEEE, New York, 1980), pp. 1-9  |

\* \* \* \* \*

## UNPUBLISHED REPORTS

Journal ArticlesJA No.

- |      |  |   |                                       |
|------|--|---|---------------------------------------|
| 5019 | Doppler-Limited Spectroscopy of the $3\nu_3$ Band of SF <sub>6</sub>                     | A. S. Pine<br>A. G. Robiette*             | Accepted by J. Mol. Spectrosc.        |
| 5040 | The Effect of Implant Temperature on the Electrical Characteristics of Ion Implanted InP | J. P. Donnelly<br>C. E. Hurwitz           | Accepted by Solid-State Electron.     |
| 5043 | Pump Depletion and Saturation of Two-Photon Resonant Third-Harmonic Generation Processes | H. Kildal<br>S. R. J. Brueck              | Accepted by IEEE J. Quantum Electron. |
| 5049 | Deconvolution of Infrared Spectra Beyond the Doppler Limit                               | J. Pliva*<br>A. S. Pine<br>P. D. Willson* | Accepted by Appl. Opt.                |
| 5051 | The Electrical Characteristics of InP Implanted with the Column IV Elements              | J. P. Donnelly<br>G. A. Ferrante          | Accepted by Solid-State Electron.     |

---

\* Author not at Lincoln Laboratory.



<u>JA No.</u>			
5059	Stoichiometric Lasers	S. R. Chinn	Accepted for <u>Handbook Series on Laser Science &amp; Technology, Vol. I: Lasers in All Media</u> (CRC Press, Inc., West Palm Beach, Florida)
5065	Ohmic Contact Formation on InP by Pulsed Laser Photochemical Doping	T. F. Deutsch D. J. Ehrlich R. M. Osgood, Jr. Z. L. Liao	Accepted by Appl. Phys. Lett.
5068	Direct Writing of Regions of High Doping on Semiconductors by UV-Laser Photodeposition	D. J. Ehrlich R. M. Osgood, Jr. T. F. Deutsch	Accepted by Appl. Phys. Lett.
5074	One-Step Repair of Transparent Defects in Hard-Surface Photolithographic Masks via Laser Photodeposition	D. J. Ehrlich T. F. Deutsch D. J. Silversmith R. M. Osgood, Jr.	Accepted by IEEE Electron Devices Lett.
5075	Picosecond Optical Sampling	H. A. Haus* S. T. Kirsch* K. Mathyssek* F. J. Leonberger	Accepted by IEEE J. Quantum Electron.
5082	Generation of Ultrashort Pulses in Synchronous Pumping of Near-Millimeter Wave Lasers	W. Lemley* A. V. Nurmikko* B. J. Clifton	Accepted by Intl. J. Infrared and Millimeter Waves
5084	Laser Sources and Detectors for Guided Wave Optical Signal Processing	I. Melngailis	Accepted by Opt. Eng.
5087	Far Infrared Heterodyne Detectors	P. E. Tannenwald	Accepted by Intl. J. Infrared and Millimeter Waves
5090	Long Wavelength Semiconductor Diode Lasers	I. Melngailis	Accepted in <u>McGraw-Hill 1984 Yearbook of Science and Technology</u>
5091	Convolver Technology for Spread Spectrum Communications	S. A. Reible	Accepted by IEEE Trans. Microwave Theory Tech.
5093	High-Temperature cw Operation of GaInAsP/InP Lasers Emitting at 1.5 $\mu\text{m}$	J. J. Hsieh	Accepted by Appl. Phys. Lett.
5096	Atomic Resonance-Line Lasers: New Sources for Analytical Atomic Spectrometry	D. J. Ehrlich R. M. Osgood, Jr. G. C. Turk* J. C. Travis*	Accepted by Anal. Chem.
5108	High-Speed Operation of LiNbO <sub>3</sub> Electrooptic Interferometric Waveguide Modulators	F. J. Leonberger	Accepted by Opt. Lett.

---

\* Author not at Lincoln Laboratory.

JA No.

5109

Crystallization Front Velocity  
During Scanned Laser Crystallization of Amorphous Ge FilmsR. L. Chapman  
J. C. C. Fan  
H. J. Zeiger  
R. P. Gale

Accepted by Appl. Phys. Lett.

Meeting Speeches\*MS No.4530B,  
CHigh-Resolution Molecular  
Spectroscopy Using a Tunable  
Difference-Frequency Laser  
Source

A. S. Pine

Seminars: Sandia Laboratory,  
Albuquerque, New Mexico,  
23 April 1980; Los Alamos  
Scientific Laboratory,  
Los Alamos, New Mexico,  
24 April 19804584C,  
DSchottky Diodes and Their  
Application to Spectroscopy

H. R. Fetterman

Seminars: Raytheon, Waltham,  
Massachusetts, 6 February  
1980; University of Massa-  
chusetts, Amherst, 10 March  
1980

4878C

Liquid Phase Epitaxy of  
 $\text{Hg}_{1-x}\text{Cd}_x\text{Te}$ 

T. C. Harman

2nd BACG Mtg. on "The  
Crystal Growth & Character-  
isation of II-VI Compounds,"  
University of Lancaster,  
England, 14-16 April 1980

4894B

Efficient GaAs Shallow-  
Homojunction Solar Cells on  
Single-Crystal GaAs and Ge  
Substrates

J. C. C. Fan

Centro de Investigacion y de  
Estudios Avanzados del I.P.N.,  
Mexico City, Mexico, 7 Febru-  
ary 1980

4959A

Surface-Acoustic-Wave  
Devices for Processing  
Spread-Spectrum Signals

R. C. Williamson

Electrical Engineering Semi-  
nar, University of Pennsyl-  
vania, 6 March 1980

4960B

High-Speed InP Optoelectronic  
Sampling Device

F. J. Leonberger

Workshop on High-Speed A/D  
Conversion, Portland, Oregon,  
11 February 1980

4967A

Graphoepitaxy of Silicon on  
Amorphous Substrates

H. I. Smith

5223

A Precision Technique for  
Fabrication of Simple Metallic  
Microstructures with  $<100 \text{ \AA}$   
DimensionsA. E. White<sup>†</sup>  
D. C. FlandersAmerican Physical Society  
Mtg., New York, New York,  
24-28 March 1980

5225

Measurement of Spin-Orbit  
Splitting  $\Delta_0$  in InP at 77 K  
Using ElectoreflectanceK. Alavi<sup>†</sup>  
R. L. Aggarwal<sup>†</sup>  
S. H. Groves

5000A

Magnetism and Chemical  
Reactions

H. J. Zeiger

Material Science Colloq.,  
M.I.T., 8 February 1980

\* Titles of Meeting Speeches are listed for information only. No copies are available for distribution.

<sup>†</sup> Author not at Lincoln Laboratory.

MS No.

5152A	Laser Induced Photochemical Reactions for Electronic Device Fabrication	D. J. Ehrlich T. F. Deutsch R. M. Osgood, Jr.	Seminar, Xerox Corporation, Rochester, New York, 9 May 1980
5196	Electrode Band Structure and Interface States in Photo-electrochemical Cells	J. G. Mavroides J. C. C. Fan H. J. Zeiger	Photoeffects at Semiconductor-Electrolyte Interfaces Symp., Houston, Texas, 25 March 1980
5228	High-Temperature cw Operation of GaInAsP/InP Lasers Emitting at 1.5 $\mu$ m	J. J. Hsieh	Topical Meeting on Integrated and Guided-Wave Optics, Incline Village, Nevada, 28-30 January 1980
5235A	Laser Photochemical Techniques for Semiconductor Processing	T. F. Deutsch	North Central Chapter of American Vacuum Society, Detroit, Michigan, 8 May 1980
5247A	Artificial Microstructures for Integrated Electronics	H. I. Smith	Applied Physics Seminar, California Institute of Technology, Pasadena, 1 February 1980
5250	Application of Artificial Microstructures to Chemistry	H. I. Smith	Chemistry Seminar, M.I.T., 12 February 1980
5250A, B	Submicrometer Structures Research & Applications	H. I. Smith	Seminars: Digital Equipment Corporation, Westboro, Massachusetts, 10 April 1980; College of the Holy Cross, Worcester, Massachusetts, 26 March 1980
5252	GaAs Monolithic Balanced Mixer and Monolithic MESFET Amplifier	A. Chu W. Courtney G. Lincoln L. Mahoney R. Sudbury	Workshop on Compound Semiconductors for Microwave Materials and Devices, San Francisco, California, 11-12 February 1980
5259	Charge-Coupled Devices for Signal Processing	B. E. Burke	Seminar, Iowa State University, Ames, 4 February 1980
5266	Laser Photochemistry and Its Application to Microelectronics	R. M. Osgood, Jr.	March Mtg., IEEE Quantum Electronics, Waltham, Massachusetts, 20 March 1980
5268	Wide Bandwidth CO <sub>2</sub> Laser Photomixers	D. L. Spears	SPIE Technical Symposium East '80, Washington, D.C., 7-11 April 1980
5345	Detectors for the 1.1 - 1.6 $\mu$ m Spectral Region	C. E. Hurwitz	
5277	Far Infrared Heterodyne Systems	P. E. Tannenwald	Heterodyne Systems and Technology Conf., Williamsburg, Virginia, 25-27 March 1980
5293	Laser Sources for Heterodyne Detection	A. Mooradian	

MS No.

- |            |   |                |  |
|------------|---|----------------|--|
| 5312       | Extending the Operating Temperature, Wavelength and Frequency Response of HgCdTe Heterodyne Detectors | D. L. Spears   | Heterodyne Systems and Technology Conf., Williamsburg, Virginia, 25-27 March 1980  |
| 5290, A, B | Millimeter and Submillimeter Wave Schottky Diode Receivers  | B. J. Clifton  | Seminars: U.S. Army Electronics Research and Development Command, Fort Monmouth, New Jersey, 28 February 1980; New Jersey Chapter IEEE, Monmouth College, New Jersey, 28 February 1980; Brown University, Providence, Rhode Island, 7 March 1980 |
| 5296       | Recent Applications of Microstructure Fabrication Technology  | D. C. Flanders | Seminar, Yale University, New Haven, Connecticut, 7 March 1980   |
| 5363       | Progress in Microfabrication: Applications to 1-D Conduction Studies                                  | A. E. White    | Seminar, Middlebury College, Middlebury, Vermont, 23 April 1980  |

## ORGANIZATION

### SOLID STATE DIVISION

A. L. McWhorter, *Head*  
I. Melngailis, *Associate Head*  
J. F. Goodwin, *Assistant*  
R. H. Rediker, *Senior Staff*  
P. E. Tannenwald, *Senior Staff*

### QUANTUM ELECTRONICS

A. Mooradian, *Leader*  
P. L. Kelley, *Associate Leader*

Barch, W. E.	Fetterman, H. R.
Belanger, L. J.	Fleming, M. W.*
Blumberg, W. A. M.	Hancock, R. C.
Brueck, S. R. J.	Kildal, H.
Burke, J. W.	Killinger, D. K.
Bushee, J. F., Jr.	Menyuk, N.
Chinn, S. R.	Moulton, P. F.
DeFeo, W. E.	Osgood, R. M., Jr.
Deutsch, T. F.	Parker, C. D.
Ehrlich, D. J.	Peck, D. D.
Feldman, B.	Pine, A. S.

### ELECTRONIC MATERIALS

A. J. Strauss, *Leader*  
H. J. Zeiger, *Associate Leader*  
J. G. Mavroides, *Senior Staff*

Anderson, C. H., Jr.	Heich, J. J.
Button, M. J.	Iseler, G. W.
Chapman, R. L.	Kafalas, J. A.
Davis, F. M.	Kolesar, D. F.
Delaney, E. J.	Krohn, L., Jr.
Fahey, R. E.	Mastromattei, E. L.
Fan, J. C. C.	Owens, E. B.
Finn, M. C.	Palm, B. J.
Flutie, R. E.	Pantano, J. V.
Foley, G. H.	Salerno, J. P.*
Gale, R. P.	Tracy, D. M.
Hong, H. Y-P.	Vohl, P.

### APPLIED PHYSICS

R. C. Williamson, *Leader*  
C. E. Hurwitz, *Associate Leader*  
T. C. Harman, *Senior Staff*  
R. H. Kingston, *Senior Staff*

Armiento, C. A.*	Leonberger, F. J.
Calawa, A. R.	Liau, Z-L.
Carter, F. B.	Lind, T. A.
DeMeo, N. L., Jr.	McBride, W. F.
Diadiuk, V.	Paladino, A. E.
Donnelly, J. P.	Plonko, M. C.
Duffy, P. E.	Spears, D. L.
Ferrante, G. A.	Tsang, D. Z.*
Foyt, A. G.	Turner, G. W.
Groves, S. H.	Walpole, J. N.
Kirsch, S. T.*	

### ANALOG DEVICE TECHNOLOGY

E. Stern, *Leader*  
J. H. Cafarella, *Assistant Leader*  
R. W. Ralston, *Assistant Leader*

Anderson, A. C.	Kernan, W. C.
Armenault, D. R.	Leung, I.
Baker, R. P.	Lynch, J. T.
Becker, R. A.	Oates, D. E.
Behrmann, G. J.	Reible, S. A.
Brogan, W. T.	Slattery, R. L.
Dolat, V. S.	Withers, R. S.
Holtham, J. H.	Yao, I.

### MICROELECTRONICS

W. T. Lindley, *Leader*  
F. J. Bachner, *Associate Leader*  
H. I. Smith, *Assistant Leader*

Alley, G. D.	Felton, B. J.	McGonagle, W. H.
Baker, E-M.	Flanders, D. C.	Melngailis, J.†
Bozler, C. O.	Geis, M. W.	Mountain, R. W.
Burke, B. E.	Gray, R. V.	Murphy, R. A.
Chiang, A. M.	Hansell, G. L.*	Nichols, K. H.
Chu, A.	Hawryluk, A. M.*	Piacentini, W. J.
Clifton, B. J.	Jacobsen, E. H.	Pichler, H. H.
Daniels, P. J.	Lau, C-L.*	Rathman, D. D.
DeGraff, P. D.	Lincoln, G. A., Jr.	Shaver, D. C.‡
Durant, G. L.	Lyszcza, T.	Silversmith, D. J.
Economou, N. P.	Macropoulos, W.	Smythe, D. J., Jr.
Efremow, N., Jr.	Mahoney, L. J.	Sotomayor-Diaz, O.‡
Elta, M. E.	McClelland, R. W.	Wilde, R. E.

\* Research Assistant

† Part Time

‡ Staff Associate

## I. SOLID STATE DEVICE RESEARCH

### A. HIGH-SPEED OPERATION OF $\text{LiNbO}_3$ ELECTROOPTIC INTERFEROMETRIC WAVEGUIDE MODULATORS

In a previous report<sup>1</sup> the development of single-mode electrooptic interferometric modulators, which used Ti-diffused waveguides in  $\text{LiNbO}_3$ , was discussed. This type of modulator is especially well suited for wideband electrooptic analog-to-digital (A/D) conversion<sup>2-4</sup> and for picosecond optical sampling.<sup>5</sup> Here, we describe high-speed operation of these modulators. Modulation up to 1.4 GHz has been achieved and RF modulation of the 275-MHz pulse train from a CW mode-locked frequency-doubled Nd:YAG laser has been demonstrated.

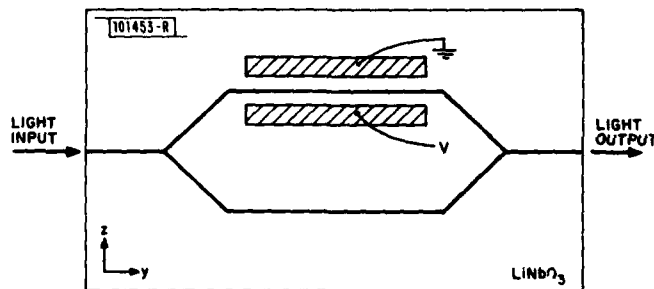


Fig. I-1. Schematic drawing of electrooptic interferometric modulator fabricated from single-mode waveguides in  $\text{LiNbO}_3$ .

A schematic drawing of the modulator, which is a waveguide version of the Mach-Zehnder interferometer, is shown in Fig. I-1. It can be shown that the modulator output intensity  $I$  varies as  $I \sim I_0 [1 + \cos(\phi + \psi_s)]/2$ , where  $I_0$  is the incident intensity,  $\phi$  is the electrooptic phase shift between the arms, and  $\psi_s$  accounts for any static phase shift between the arms. The electrooptic phase shift is given by  $\phi = \pi V/V_\pi$ , where  $V$  is the applied voltage and  $V_\pi$  is the voltage required to obtain a  $\pi$ -radian phase shift between the arms. The periodic variation of the output intensity with voltage permits one to obtain optical modulation at frequencies higher than that of the drive voltage by driving through multiple- $\pi$  phase shifts in one half period of the drive signal. In particular, a triangular drive signal of peak-to-peak voltage  $nV_\pi$  at frequency  $f$  will produce sinusoidal optical modulation at frequency  $nf$ . A sinusoidal drive signal of the form  $(nV_\pi/2) \sin 2\pi ft$  will produce an FM output. The maximum modulation rate of this output will be  $\pi nf/2$  and will occur during the linear portion of the driving sinusoid. The maximum value of  $n$  is set by breakdown voltage  $V_{BD}$  of the device, or  $n \leq 2V_{BD}/V_\pi$  for a zero-mean drive signal.

Low-frequency measurements on these devices at  $0.633 \mu\text{m}$  were previously reported.<sup>1</sup> At DC, the devices were characterized by a 17-dB extinction ratio and  $V_\pi \sim 4.5 \text{ V}$ . The output linearity of a similar device, which was driven through multiple- $\pi$  phase shifts, was measured using a 30-V triangular waveform. For this case, the CW input light was sinusoidally modulated at 130 kHz as the output was driven through  $\sim 6 \pi$ -phase shifts in one half cycle of the driving signal. Equal spacing between the zero crossings, which is indicative of good linear response, was obtained and was consistent with earlier results for multimode interferometric modulators.<sup>2,6</sup>

To determine the modulator response at high frequencies, CW 0.633- $\mu\text{m}$  light was incident on the modulator, and sinusoidal drive signals in the 9- to 39-dBm, 70- to 140-MHz range were applied to the electrodes. The resulting FM optical waveforms were detected by a fast Si avalanche photodiode. For these measurements, a 50- $\Omega$  resistor was placed in parallel with the modulator at the end of the drive cable. (The modulator had a 2-pF capacitance, implying an RC time constant of 100 psec.) The response of the device to a 34-dBm (32-V peak-to-peak) 140-MHz drive signal is shown in Fig. I-2. As can be seen, the output was driven through

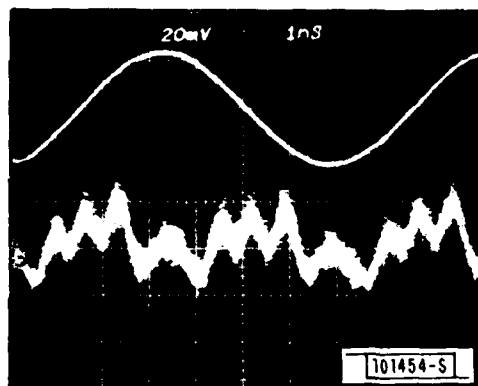
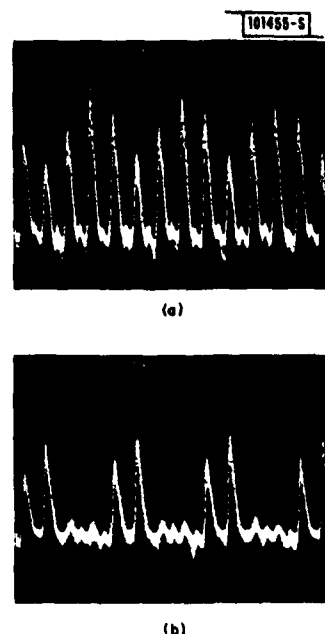


Fig. I-2. Oscillogram of (upper trace) 140-MHz 34-dBm sine wave modulator drive and (lower trace) modulator optical response for CW optical input. The optical modulation during the linear portion of the driving waveform is at 1.4 GHz.

$\sim 7 \pi$ -phase shifts in one half cycle of the driving signal. Approximately sinusoidal modulation at 1.4 GHz was obtained during the linear portion of the drive signal, with lower frequency modulation occurring during the more slowly varying portions of the drive signal. The maximum frequency of 1.4 GHz is consistent with that calculated from the previously given expression  $\pi n f / 2$  for this case of  $n = 7$ . The uneven amplitude of the detected signal is due to the bandwidth limitations of the Si detector and the output amplifier. Similar measurements made with a 70-MHz 37-dBm drive signal gave 950-MHz optical intensity modulation with nearly twice the modulation depth obtained at 1.4 GHz during the linear portion of the driving signal. It is worth noting that no time variations in output intensity or mode shape, as might be produced by optical damage, were observed.

The devices have also been used to RF-modulate a train of 275-MHz, 150-psec-wide pulses from a CW mode-locked, frequency-doubled Nd:YAG laser. (For this 0.53- $\mu\text{m}$  wavelength, the waveguides supported both  $\text{TE}_{11}$  and  $\text{TE}_{21}$  modes.) The modulator output is shown in Fig. I-3 for 68.9-MHz drive powers of 19 and 29 dBm. For these measurements, the 68.9-MHz signal was synchronized with the drive signal to the laser acoustooptic modulator to obtain a stationary display on a sampling oscilloscope. The envelope of the output pulse train follows that expected for a CW optical input and these RF power levels. A signal-to-noise ratio of at least 34 dB was obtained. The width of the detected pulses was limited by the 1.5-GHz bandwidth of an output amplifier used between the photodiode and the sampling oscilloscope. It was not possible to quantitatively fit the signal peaks to a CW output signal because the limited CW power at 0.53  $\mu\text{m}$  yielded oscillograms with relatively low signal-to-noise ratios. It should be noted that this experiment is the first demonstration of the use of mode-locked laser pulses to sample the

Fig. 1-3. Oscillograms showing modulation of 275-MHz optical pulse train from CW mode-locked, frequency-doubled Nd:YAG laser for 68.9-MHz modulator drive at (a) 19 and (b) 29 dBm.



amplitude of an analog drive signal and suggests the usefulness of the technique for the proposed electrooptic A/D converter.<sup>3,4</sup>

F. J. Leonberger

#### B. THICKNESS OF LPE $\text{Ga}_x\text{In}_{1-x}\text{As}_y\text{P}_{1-y}$ LAYERS NEARLY LATTICE-MATCHED TO (100) INP SUBSTRATES

Precise thickness control in the LPE growth of quaternary layers is required in order to realize the full potential of  $\text{Ga}_x\text{In}_{1-x}\text{As}_y\text{P}_{1-y}$ /InP optoelectronic devices. In the extreme case of InP (i.e.,  $x = y = 0$ ), the growth thickness has been studied as a function of growth-solution composition, temperature, and time.<sup>7</sup> However, only a few scattered data have been reported for the quaternary.<sup>8-11</sup> In this work, a systematic study has been carried out over the entire range of quaternary layer compositions which are nearly lattice-matched to the InP substrates ( $|\Delta a/a| \leq 0.3\%$ ).

Ten different quaternary growth-solution compositions have been used in the present work. (The growth solutions and samples were the same as those used in a previous study of the growth-temperature dependence of LPE GaInAsP/InP lattice mismatch.<sup>12</sup>) First, the liquidus temperature  $T_l$  (at which the solution and small crystallites were equilibrated) was determined to an accuracy of  $\pm 0.5^\circ\text{C}$  for each growth-solution composition. The ten  $T_l$ 's were found to exhibit a range of temperature between 639.5 and 650.5 $^\circ\text{C}$ . Then, by using the step-cooling technique,<sup>7</sup> several LPE growth runs were carried out for each growth solution. A constant growth temperature  $T_g$  was used for each LPE run. The amount of step-cooling,  $\Delta(\equiv T_l - T_g)$ , was normally between 4 and 11 $^\circ\text{C}$ ; the growth time was between 0.5 and 10 min. These growth conditions resulted in quaternary layers of 0.6- to 4.5- $\mu\text{m}$  thickness, which were measured by using an optical microscope.



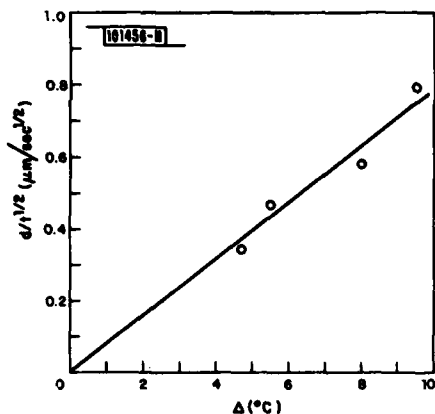


Fig. I-4. Relationship between thickness  $d$ , growth time  $t$ , and amount of step-cooling  $\Delta$  in the LPE growth of  $\text{Ga}_{0.5}\text{In}_{0.5}\text{As}$  layers on (100) InP.

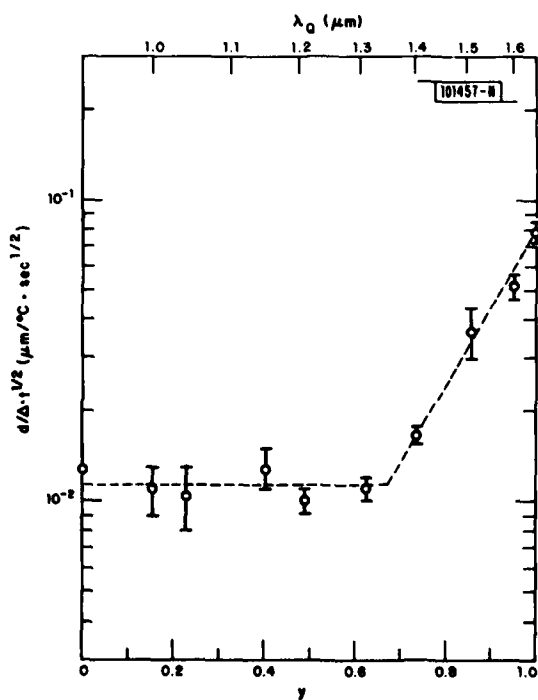


Fig. I-5. Dependence of the coefficient  $C$  (as defined in  $d = C\Delta \cdot t^{1/2}$ ) on the  $\text{Ga}_x\text{In}_{1-x}\text{As}_y\text{P}_{1-y}$  composition in the LPE growth of quaternary layers on (100) InP.

The observed layer thickness  $d$ , as a function of step cooling  $\Delta$  and growth time  $t$ , showed good agreement with the following relationship derived for the diffusion-limited growth mechanism<sup>7</sup>

$$d = C\Delta \cdot t^{1/2} \quad (1)$$

where the coefficient  $C$  is a "material constant" and is presumably a relatively slow-varying function of temperature.<sup>7</sup> The value of  $C$  for  $\text{Ga}_{0.5}\text{In}_{0.5}\text{As}$  (i.e., the extreme case of  $y = 1$ ) is obtained from the data of Fig. I-4. The slope of the line is the coefficient  $C$ , according to Eq. (1). Figure I-5 shows the experimental  $C$ -values thus determined for the entire range of quaternary compositions. The  $y$ -values in Fig. I-5 were obtained by using an empirical relationship between the quaternary wavelength  $\lambda_Q$  and composition.<sup>13</sup> A single variable  $y$  is used to specify the quaternary composition because of the relationship between  $x$  and  $y$  imposed by the lattice matching condition.<sup>13</sup>

Figure I-5 shows a nearly constant  $C$ -value for  $0.92 \mu\text{m} (\approx \lambda_{\text{InP}}) \leq \lambda_Q \leq 1.3 \mu\text{m}$ . Moreover, this  $C$ -value is in good agreement with the value obtained for the growth of InP layers.<sup>7</sup> These observations suggest that (similar to the InP growth) the phosphorus diffusion in the solution is the rate-limiting step in these growths. This agrees with the fact that phosphorus has a much larger distribution coefficient (and, therefore, will be depleted over a much longer distance from the growth front) than the other three components of the quaternary. An analogous argument may also be applied to the rise in  $C$ -value in the extreme long wavelength region in Fig. I-5, in which phosphorus is not present. (That the  $C$ -value for  $y = 1$  is nearly one order of magnitude larger than that for  $0 \leq y \leq 0.6$  agrees with the observation that gallium has a distribution coefficient one order of magnitude smaller than that of phosphorus.<sup>14</sup>)

In conclusion, we have carried out a study on the thickness of LPE  $\text{Ga}_x\text{In}_{1-x}\text{As}_y\text{P}_{1-y}$  layers as a function of growth temperature, time, and composition. Despite the system's complexity, the results were combined into a more unified picture. We believe that the present results are also very useful in the preparation of heterostructures for optoelectronic devices.

Z. L. Liao

### C. LPE SURFACE MORPHOLOGY OF $\text{InP}(\text{Zn})$

A terraced surface morphology sometimes occurs with liquid-phase epitaxial (LPE) growth on substrates misoriented from a low-index plane. The terraces usually consist of relatively wide treads of the low-index plane and narrow risers at a small angle,  $\Theta$ , to the low-index plane.  $\Theta$  does not change with the amount of misorientation, and, as a result, terrace-free growth occurs both for substrates oriented on the low-index plane and at an angle  $\Theta$  from the low-index plane, designated as the critical orientation.<sup>15,16</sup> In the case of InP LPE grown layers on InP substrates of nominal (100) orientation,  $\Theta \approx 2.6^\circ$  toward  $\langle 100 \rangle$  (Ref. 17).

We have found that the terraced morphology is characteristic of InP growth in some, but not all, situations. Terraced growth occurs for layers that are heavily doped with Zn ( $N_A \geq 5 \times 10^{17} \text{ cm}^{-3}$ ). A photomicrograph of growth with  $N_A \approx 1 \times 10^{18} \text{ cm}^{-3}$  on a nominally oriented (100) substrate is shown in Fig. I-6(a), and the terrace morphology is evident. Growth from the same solution but using a substrate nominally oriented  $2.6^\circ$  off the (100) in a  $\langle 110 \rangle$  direction gives a smoother and markedly different morphology as shown in Fig. I-6(b). The closely spaced terraces of Fig. I-6(b) are what would be expected if the substrate were oriented at slightly less than  $\Theta$  from the low-index plane.

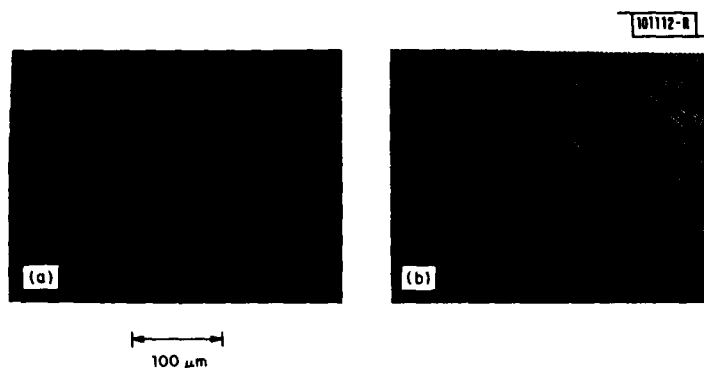


Fig. 1-6. Photomicrographs of growth from a Zn-doped solution (giving  $N_A \approx 1 \times 10^{18} \text{ cm}^{-3}$ ) with (a) a substrate of nominal (100) orientation and (b) a substrate nominally oriented at  $2.6^\circ$  off (100).

For not intentionally doped and Sn-doped growth, there is only slight evidence of terraced growth. Little or no improvement in smoothness results in these cases from using substrates that are either accurately oriented to (100) (within  $0.1^\circ$ ) or oriented  $2.6^\circ$  off (100). Our growths are usually made within the temperature range of  $630^\circ$  to  $700^\circ\text{C}$ ; they are initiated with a supercooling of  $5^\circ$  to  $10^\circ\text{C}$  and are grown at a cooling rate of  $0^\circ$  to  $0.7^\circ\text{C/M}$ . The results for the undoped and Sn-doped growths seem to suggest that, under these conditions, morphology defects are not related to the terracing phenomena. This is apparently similar to the case of GaAs(Sn) where even small amounts of supercooling tend to eliminate terracing.<sup>18</sup>

From these preliminary results, it would seem for the case of LPE InP(Zn) growth that efforts to orient substrates accurately to (100) or nominally to the critical orientation should result in improved morphology. There are two minor disadvantages to using the  $2.6^\circ$ -off orientation (critical orientation): (1) if a meltback with an indium solution is used, the etched surface is not as smooth as for nominally oriented (100) substrates; and (2) if too large a deviation from the (100) occurs, nucleation problems with resulting island growth are seen. This is most likely to be a problem with substrates that have edge rounding due to etching.

S. H. Groves  
M. C. Plonko

#### D. LIQUIDUS MEASUREMENTS IN THE Te-CORNER OF THE Hg-Cd-Te PHASE DIAGRAM

In order to use the liquid phase epitaxial (LPE) technique for the preparation of  $\text{Hg}_{1-x}\text{Cd}_x\text{Te}$  layers, data on the phase diagram are required. Both differential thermal analysis (DTA) and the method of direct, visual observation<sup>19,20</sup> of the surface of the LPE growth solutions just prior to epitaxial growth were considered. The DTA method was used in the initial work and the results<sup>21</sup> were reported. The DTA experiments revealed unusually large supercooling effects for Te-rich Hg-Cd-Te solutions. Although the usual corrections were carried out for supercooling, the liquidus temperatures from DTA were not considered sufficiently precise for the further development of the LPE techniques. The LPE method was not used because the temperature at which the last bit of surface solid melts upon slow heating may not correspond to the last bit of solid in the solution bin and hence may not correspond to the liquidus temperature.

In order to eliminate possible errors due to supercooling with DTA and belated non-surface dissolution of solid in the LPE method, a modified direct observational (MDO) technique was devised. A schematic diagram of the MDO apparatus is shown in Fig. I-7. Each sample is prepared by placing the required amounts of high-purity Hg, CdTe, and Te totaling 80 g in an evacuated (by a diffusion pump), then sealed, quartz ampoule. The sample is placed in a transparent furnace at a temperature 20° to 30°C above the anticipated melting point. Ceramic fiber is packed around and inside the inner quartz tube as illustrated in Fig. I-7. After homogenization of the components for about 24 hr, the sample is forced-air quenched. The sample tube, which is placed in the slight horizontal temperature gradient depicted in Fig. I-8, is heated rapidly to an average temperature about 20°C below the estimated liquidus temperature. Then the furnace temperature is increased gradually in increments of 1° to 5°C/day. Temperatures are measured with Platinel thermocouples. Initially, large quantities of solid are present below the liquid surface and along the bottom of the sample tube. To observe the solid visually, the quartz ampoule containing the Hg-Cd-Te sample is rotated through 180 deg. As the liquidus temperature is approached, the solid is reduced to a thin layer approximately 1 mm<sup>2</sup> in area at the position indicated schematically by the dark spot in Fig. I-8. Heating is continued until a final increase of 1°C in furnace temperature causes complete dissolution of the solid. The liquidus temperature is taken as the final temperature plus a thermocouple correction term, which was obtained in the following manner. The melting point of InSb was measured by MDO using the apparatus and procedure described. The difference between the measured value of 528°C and the literature value of 525°C was used as the correction term, i.e., 3°C.

The results of the MDO measurements for various  $(\text{Hg}_{1-x}\text{Cd}_x)_{1-y}\text{Te}_y$  compositions are given in Table I-1. Each liquidus temperature listed was obtained after a minimum of 7 days of incremental temperature changes. Using the data of Table I-1, the liquidus sections of the temperature-composition phase diagram for the Te-rich portion of the Hg-Cd-Te system are shown for  $x = 0.0, 0.05, 0.10, \text{ and } 0.20$  in Fig. I-9. The  $y = 0.5$  points are taken from the liquidus curve of Blair and Newnham<sup>22</sup> for the  $\text{Hg}_{1-x}\text{Cd}_x\text{Te}$  pseudobinary. The  $(\text{Hg}_{1-x}\text{Cd}_x)_{1-y}\text{Te}_y$ -Te eutectic compositions have not been determined by MDO. The MDO results are not in good agreement with the partial liquidus diagram for HgTe given in the 1958 edition of Hansen.<sup>23</sup> However, the HgTe data for  $y \leq 0.75$  are in excellent agreement with the 1965 HgTe phase diagram of Strauss and Brebrick<sup>24</sup> obtained by DTA. For  $y > 0.75$ , the MDO results are significantly higher, presumably because supercooling has been eliminated as a source of error. The interpolated liquidus temperature values from Fig. I-9 are 13° to 15°C higher than the values for two ternary  $\text{Hg}_x\text{Cd}_y\text{Te}_z$  compositions that were obtained by Bowers *et al.*<sup>25</sup> from LPE growth experiments.

T. C. Harman

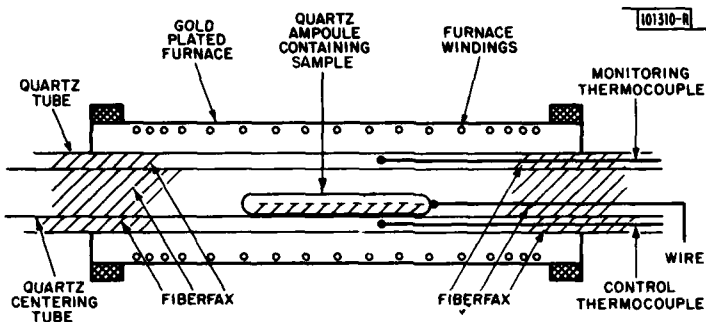


Fig. I-7. Schematic of the direct observation apparatus used to measure liquidus temperatures of the Te-rich HgCdTe phase diagram.

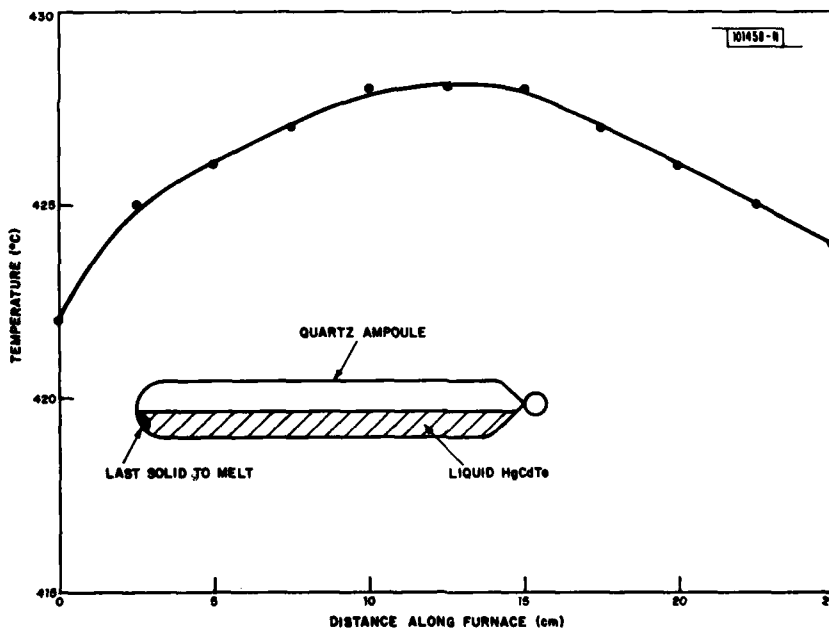
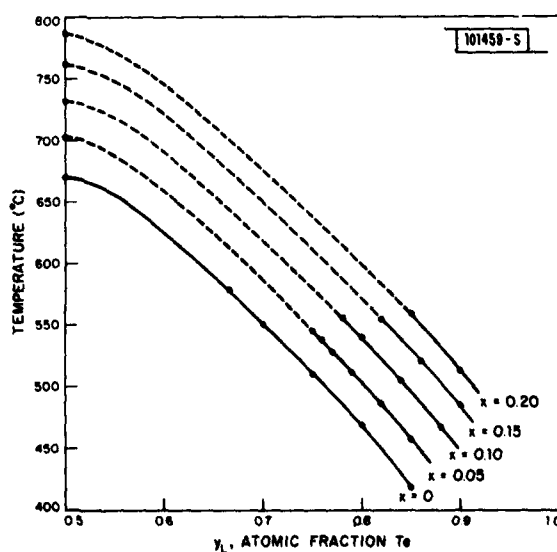


Fig. I-8. Temperature vs distance along section of furnace used to measure liquidus points by the MDO technique.

TABLE I-1 TEMPERATURES FOR THE LAST SOLID TO MELT WHEN HEATING VARIOUS TWO-PHASE MIXTURES OF $(\text{Hg}_{1-x}\text{Cd}_x)_1\text{Te}_y$ (from MDO Data)		
$x, \text{Cd}$	$y, \text{Te}$	$T, (^\circ\text{C})$
0	0.665	579
0	0.70	550
0	0.75	510
0	0.80	469
0	0.85	418
0.05	0.75	545
0.05	0.76	538
0.05	0.77	528
0.05	0.79	512
0.05	0.82	487
0.05	0.85	458
0.10	0.78	556
0.10	0.80	541
0.10	0.84	506
0.10	0.88	468
0.15	0.82	555
0.15	0.86	521
0.15	0.90	485
0.20	0.85	559
0.20	0.90	513

Fig. I-9. Partial phase diagram  
of  $(\text{Hg}_{1-x}\text{Cd}_x)_1\text{Te}_y$ .



## REFERENCES

1. F. J. Leonberger, Solid State Research Report, Lincoln Laboratory, M.I.T. (1979:3), p. 4.
2. H. F. Taylor, M. J. Taylor, and P. W. Bauer, Appl. Phys. Lett. 32, 559 (1978).
3. H. F. Taylor, IEEE J. Quantum Electron. QE-15, 210 (1979).
4. F. J. Leonberger, C. E. Woodward, and D. L. Spears, Solid State Research Report, Lincoln Laboratory, M.I.T. (1979:2), p. 9, DDC AD-A078676/4.
5. H. A. Haus, S. T. Kirsch, K. Mathyssek, and F. J. Leonberger (to be published in IEEE J. Quantum Electron., August 1980).
6. T. R. Ranganath and S. Wang, IEEE J. Quantum Electron. QE-13, 290 (1977).
7. J. J. Hsieh, in Gallium Arsenide and Related Compounds (St. Louis) 1976, L. F. Eastman, Ed. (The Institute of Physics, Bristol and London, 1977), p. 74.
8. K. Sakai, S. Akiba, T. Yamamoto, Jpn. J. Appl. Phys. 16, 2043 (1977).
9. Y. Itaya, Y. Suematsu, S. Katayama, K. Kishino, S. Arai, Jpn. J. Appl. Phys. 18, 1795 (1979).
10. S. Akiba, K. Sakai, Y. Matsushima, T. Yamamoto, Jpn. J. Appl. Phys. 19, L79 (1980).
11. M. Feng, L. W. Cook, M. M. Tashima, and G. E. Stillman, J. Electron. Mater. 9, 241 (1980).
12. Z. L. Liau, J. J. Hsieh, T. A. Lind, D. E. Mull, and J. N. Walpole, to be published in Solid State Research Report, Lincoln Laboratory, M.I.T. (1980:1).
13. R. E. Nahory, M. A. Pollack, W. D. Johnston, Jr., R. L. Barns, Appl. Phys. Lett. 33, 659 (1978).
14. M. Feng, T. H. Windhorn, M. M. Tashima, and G. E. Stillman, Appl. Phys. Lett. 32, 758 (1978).
15. D. L. Rode, Phys. Stat. Sol. (a) 32, 425 (1975).
16. D. L. Rode, W. R. Wagner, and N. E. Schumaker, Appl. Phys. Lett. 30, 75 (1977).
17. R. Messham and A. Majerfeld, Abstract 21st Electronics Materials Conference, Boulder, Colorado, June 1979, p. 31.
18. N. Toyoda, M. Mihara, and T. Hara, Jpn. J. Appl. Phys. 18, 2207 (1979).
19. M. B. Panish, J. Electrochem. Soc. 117, 1202 (1970).
20. J. J. Hsieh, Solid State Research Report, Lincoln Laboratory, M.I.T. (1974:3), p. 25, DDC AD-A001595/8.
21. T. C. Harman, Infrared Components Final Report, Lincoln Laboratory, M.I.T. (30 September 1979).
22. J. Blair and R. Newnham, Metallurgy of Elemental and Compound Semiconductors, Vol. 12 (Interscience Publishers, New York, 1961), p. 393.
23. M. Hansen, Constitution of Binary Alloys (McGraw-Hill, New York, 1958), p. 840.
24. A. J. Strauss and R. F. Brebrick, quoted in review article by T. C. Harman published in Physics and Chemistry of II-VI Compounds, M. Aven and J. S. Prener, Eds. (North Holland, Amsterdam, 1967), p. 774.
25. J. E. Bowers, J. L. Schmit, C. J. Speersneider, and R. B. Maciolek, IEEE Trans. Electron. Devices ED-27, 24 (1980).

## II. QUANTUM ELECTRONICS

### A. LASER REMOTE SENSING OF $C_2H_4$

The differential-absorption LIDAR (DIAL) system previously used to detect CO and NO (Refs. 1, 2) has been modified to include a high-speed digital data acquisition system, and this new system has been used for the remote sensing of ethylene ( $C_2H_4$ ) in the atmosphere. Using backscattered LIDAR returns from topographic targets at ranges up to 2.7 km, we have observed the presence of  $C_2H_4$  over a busy airfield, measured its average atmospheric concentration, and investigated the effect of atmospheric turbulence on the statistical properties of the returned LIDAR signal as a function of range, atmospheric conditions, and absorbing species.

An important feature of the modified DIAL system is the use of a dual-computer data acquisition system employing integrating A/D converters. This system is capable of providing a real-time graphic display of the LIDAR data as well as the statistical analysis of a large number of pulses over a short time span. The system performs the signal averaging and statistical analysis of the normalized LIDAR returns on a pulse-to-pulse basis as well as the simultaneous comparison of the DIAL data with differential-absorption data of known gas species. The data acquisition and processing rate for the entire normalization, averaging, statistical analysis, and graphical display process permits the obtaining of a pair of 1000-pulse histograms, including printout, in approximately 20 sec. Simple averaging and display, including normalization, can be carried out in real time at the maximum pulse repetition rate (500 Hz) of our LIDAR system.

Figure II-1 shows representative histograms obtained from 1000 successive pulses of the normalized LIDAR returns from a topographic target at a range of 2.7 km, along with the signals received by simultaneously passing a small fraction of the laser beam through a 50-cm laboratory absorption cell containing 470 ppm of  $C_2H_4$  in air. The upper histogram pair in Fig. II-1 was obtained using the P(12)  $CO_2$  laser transition near  $10.513\ \mu m$ , and the lower histogram pair was obtained with the P(14) transition near  $10.532\ \mu m$ , which is coincident with an absorption transition<sup>3,4</sup> of  $C_2H_4$ . The differential absorption seen in Fig. II-1 between the off-resonance P(12) values and the on-resonance P(14) values for the laboratory absorption cell and the LIDAR returns corresponds to an average atmospheric  $C_2H_4$  concentration of approximately 60 ppb.

Figure II-2 shows the measured diurnal concentration of  $C_2H_4$  observed over a busy airfield. The data obtained on 12 March indicate an average  $C_2H_4$  concentration that reached a maximum value near 70 ppb. However, the observed  $C_2H_4$  concentration under identical LIDAR conditions on 13 March yielded a background concentration throughout the day on the order of 7 to 10 ppb. No obvious changes in the frequency of aircraft takeoffs or landings were noticed between the two days. However, there was a strong shift in the wind patterns; on 12 March the wind direction was from the airfield directly toward the observation site (wind speed 15-20 mph), and on 13 March the wind direction was reversed (wind speed 10-15 mph). This strong correlation with wind direction is to be expected since our system measures the average concentration over the entire path length, and the primary  $C_2H_4$  source is presumed to be aircraft emission at the airfield.

We have also detected the increase in  $C_2H_4$  concentration over a busy traffic roadway at a range of 500 m. Detected concentrations of  $C_2H_4$  varied from an average ambient background level of 20 ppb to values in the range of 100 to 250 ppb during peak traffic conditions.

D. K. Killinger  
N. Menyuk  
W. DeFeo



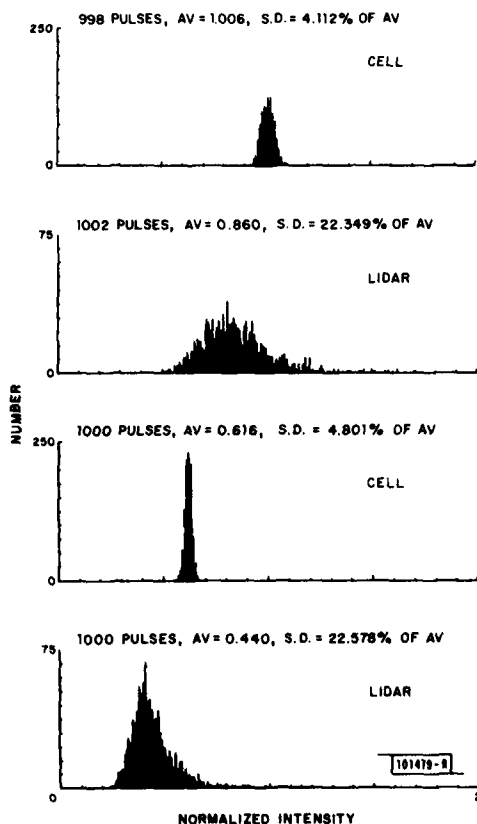


Fig.II-1. Histogram of normalized LIDAR returns and absorption ( $C_2H_4$ ) cell signals for 1000 successive pulses. Upper pair obtained using P(12)  $CO_2$  laser transition which is resonant with ethylene absorption line. Lower pair obtained using nonresonant P(14)  $CO_2$  laser line. The observed differential absorption corresponds to an average ethylene concentration of 60 ppb over the 2.7-km path.

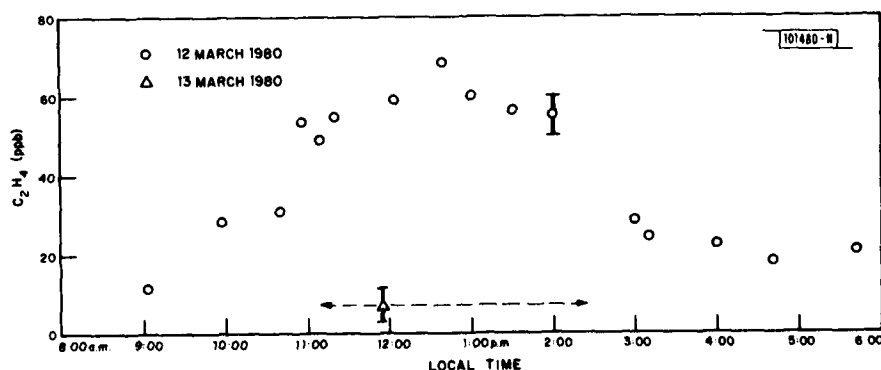


Fig.II-2. Measured diurnal variation of average ethylene concentration over a 2.7-km path to an active airfield on two different days. Strong differences were found to correlate with wind direction, as documented in text.

## B. OPTICALLY PUMPED Ce:LaF<sub>3</sub> LASER AT 286 nm

Efficient broadband fluorescence in the UV and VUV wavelength regions has been observed from a number of impurity-doped crystals and glasses,<sup>5</sup> making such materials attractive for tunable lasers. The newly discovered Ce:YLF laser,<sup>6,7</sup> based on the 4f-5d transitions of Ce<sup>3+</sup>, has served to confirm much of this promise by demonstrating high-power output and tunability in the 306- to 330-nm region. The same 4f-5d transitions used in this laser are shifted dramatically in wavelength for other host crystals, as the positions of the Ce<sup>3+</sup> energy levels are strongly crystal-field dependent. The spectroscopy of Ce<sup>3+</sup> in these other materials has been studied extensively in connection with applications of Ce<sup>3+</sup>-doped liquids and solids as electro- and photo-luminescent phosphors.<sup>8,9</sup> From these studies it is apparent that Ce<sup>3+</sup>-doped fluoride crystals and glasses are particularly attractive for laser purposes since the Ce<sup>3+</sup> emission, in many cases, falls in a wavelength region beyond the UV cutoff of organic dye lasers. This is a region of particular importance for applications in remote detection of several basic molecular species in the atmosphere, e.g., O<sub>3</sub>, SO<sub>2</sub>, and OH.

The operation of an optically pumped Ce:LaF<sub>3</sub> laser is reported here. This laser operates at the shortest wavelength yet obtained in any solid-state material. In addition, these results show that Ce<sup>3+</sup> laser operation is not confined to the single previously demonstrated host, YLF. The latter point is noteworthy since two previous studies have found pronounced excited-state absorption which will apparently prohibit laser action on the 4f-5d Ce<sup>3+</sup> transitions in YAG.<sup>10,11</sup> The spectroscopic properties of Ce:LaF<sub>3</sub> have been previously studied in order to determine the potential of this system for laser emission,<sup>12,13</sup> although no previous attempt to obtain laser action has been reported.

The unpolarized near-UV absorption and emission spectra for a 0.05% Ce-doped LaF<sub>3</sub> crystal are shown in Fig. II-3. The transitions involved are between the low-lying Ce<sup>3+</sup> 4f levels and five crystal-field-split components of the 5d state. The latter interact strongly with the lattice phonons, broadening the 4f-5d transitions. Phonon structure is not apparent at room temperature. A careful examination was made of polarization effects in emission, since these

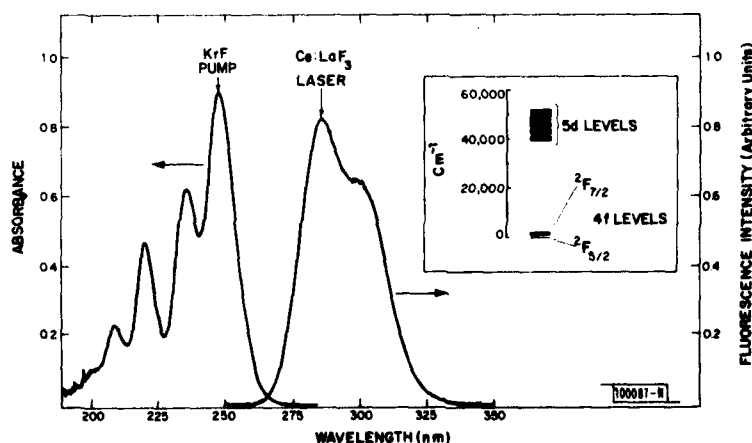


Fig. II-3. Ultraviolet absorption and spontaneous emission of a 700- $\mu$ m-thick LaF<sub>3</sub> crystal with 0.05 atomic percent Ce<sup>3+</sup> doping. For both spectra, the crystal c-axis was oriented perpendicular to the direction of observation. The KrF-pump source and Ce:LaF<sub>3</sub> laser wavelengths are indicated. The Ce<sup>3+</sup> energy levels giving rise to the spectra are shown in the inset.

are important in the operation of the Ce:YLF laser. It was found that the 285-nm/300-nm band ratio in Ce:LaF<sub>3</sub> is increased by ~3% in  $\pi$  relative to  $\sigma$  polarization; this is a much smaller effect than that seen in Ce:YLF. The Stokes shift in Ce:LaF<sub>3</sub> at 0.05% doping is 5100 cm<sup>-1</sup>. The quantum yield of fluorescence has been previously measured<sup>13</sup> to be 0.90 and shown<sup>12</sup> to be independent of temperature from 77 to 300 K.

Because of rapid internal relaxation to the lowest 5d state, the fluorescence spectrum was not noticeably different for ArF (193 nm), KrF (249 nm), or frequency-doubled Ar<sup>+</sup> laser (257 nm) pumping. Similarly, the fluorescence lifetime was identical for 249- or 193-nm excitation. For the 0.05%-doped crystal the lifetime was  $18 \pm 2$  nsec, in good agreement with the previously measured value of 20 nsec.<sup>12</sup>

Laser action was obtained in the configuration shown in Fig. II-4. A 5- × 5- × 14-mm parallelepiped with ends parallel to ~1 mrad was cut from the same crystal discussed above. A 2.5-cm-long optical cavity was formed between two 10-cm-radius dielectric mirrors, one with a reflectance of 89%, the other of 97% at 285 nm. The crystal was oriented as shown, with the c-axis perpendicular to the cavity axis. The output of a small commercial excimer laser, producing 40 mJ at 249 nm or 10 mJ at 193 nm in a 25-nsec (FWHM) pulse, was used for optical pumping. A 90-mm-focal-length quartz cylinder lens was used to focus this radiation to a 1- × 9-mm area on the crystal face. As determined by both low- and high-power measurements, the Ce:LaF<sub>3</sub> absorption length was 300  $\mu$ m at 249 nm. The pump power was varied with glass attenuators.

With KrF pumping, the Ce:LaF<sub>3</sub> laser threshold was determined by a sharp nonlinear increase in output at incident pump energies exceeding ~3 mJ, corresponding to a deposited energy density of 0.4 J/cm<sup>2</sup>. Emission was centered at 285.5 nm, at the peak of the fluorescence spectrum, and occurred in a bandwidth of ~1 nm FWHM. In this free-running mode of operation,

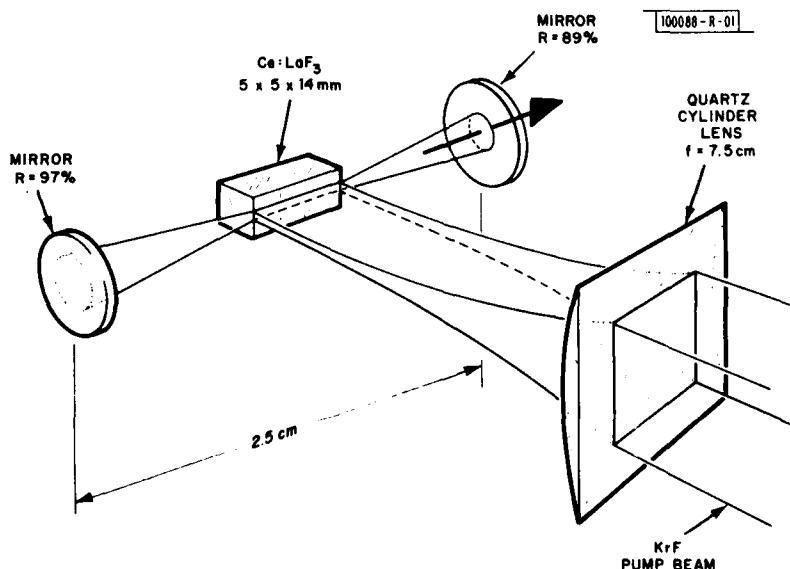


Fig. II-4. Configuration of Ce:LaF<sub>3</sub> laser.

the laser output was observed to be strongly  $\pi$ -polarized, which is consistent with the polarization of the spontaneous emission mentioned above. The stimulated emission pulse had a duration of 6 to 8 nsec FWHM and an energy, under full pumping, of  $\sim 5 \mu\text{J}$ .

D. J. Ehrlich  
P. F. Moulton  
R. M. Osgood, Jr.

### C. ONE-STEP REPAIR OF TRANSPARENT DEFECTS IN HARD-SURFACE PHOTOLITHOGRAPHIC MASKS VIA LASER PHOTODEPOSITION

An important problem in generation and use of hard-surface masks for photolithography is the elimination of defects in the mask metallization pattern. The defects can involve both local areas of undesired metallization or bridging (due to sensitizer variability, underdevelopment, underexposure, or particulate contamination) and breaks in the pattern (due to local resist failure, excessive development or exposure). A satisfactory method, based on laser vaporization,<sup>14</sup> exists for removal of excess metallization (an opaque defect). The accepted technique for correcting insufficient metallization (a transparent defect) uses a multistep photolithographic process<sup>15</sup> involving sputtering and lift-off. This procedure for the removal of transparent defects is time consuming and cumbersome.

Here we describe one-step repair of transparent mask defects using the recently developed technique of UV laser photodeposition of metals.<sup>16</sup> The technique involves illuminating a defect in a mask with focused light from a low-power UV laser. The mask is enclosed in a gas cell containing a mixture of He (or other inert gas) and a metal alkyl, at atmospheric pressure. Gas-phase photodecomposition of metal alkyl then produces a localized, adherent film of metal on the illuminated area. Since the repair function can be accomplished with the same optical system as that used to locate the defect and since no subsequent processing of the film is needed, this technique offers significant advantages in simplicity over the current technique. In addition, the demonstrated resolution limit of the process,  $\sim 1 \mu\text{m}$ , (Ref. 17) is compatible with repair of VLSI masks.

The UV laser source was a frequency-doubled  $\text{Ar}^+$  laser which produced 1 mW at 257 nm, although other commercial lasers, including pulsed excimer lasers and CW lasers at longer UV wavelengths, have also been shown to be effective sources for photodeposition. This laser output was focused with a 7.5-cm focal-length lens to a point beyond the mask substrate. The beam was located on the substrate by use of a 50X microscope which was aligned at a  $30^\circ$  angle with respect to the laser-beam axis. The demonstration mask consisted of broken chromium lines of varying widths and 100 nm thickness on a quartz substrate. Quartz was used in this experiment to aid in diagnosing the deposition<sup>16</sup>; however, masks on conventional soda-lime glass substrates can readily be repaired by this process.

Figure II-5 shows a repair on a defect, the size of which,  $50 \mu\text{m}$ , allowed it to be easily located with the low-magnification microscope in our apparatus. In this case, the repair was effected by scanning the mask in a plane normal to the  $50\text{-}\mu\text{m}$ -wide incident beam. Figure II-5(a) shows the repair in reflection, while Fig. II-5(b) shows the same object in transmission. Notice that the repair itself is both opaque and free of transparent defects. We estimate the cadmium deposits to be  $\sim 150 \text{ nm}$  thick. The striations in the deposit, which are visible in Fig. II-5(a), are the result of beam nonuniformities due to Fresnel diffraction,<sup>16</sup> which can be removed readily, if desired, with standard optical techniques.

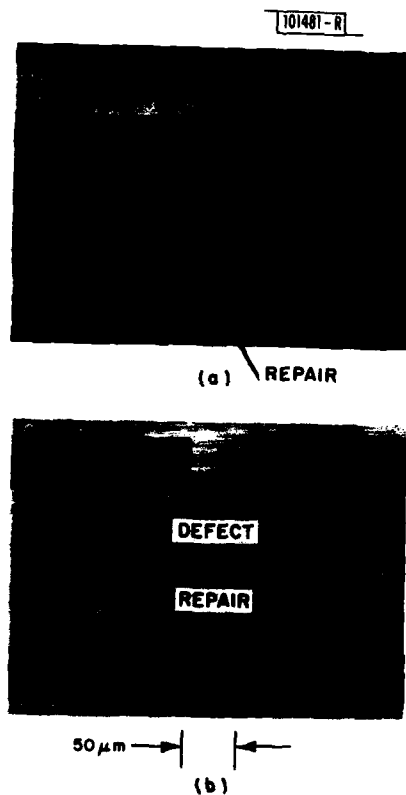
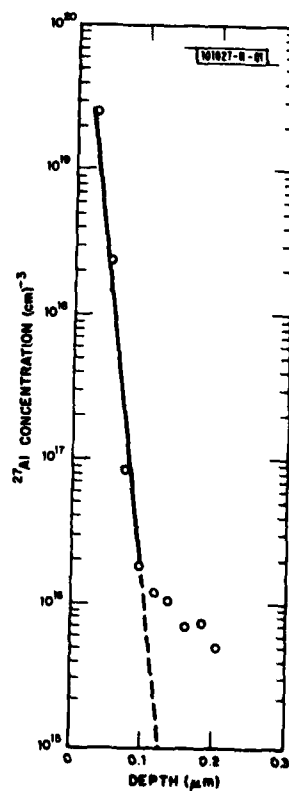


Fig. II-5. Optical micrograph of stimulated photolithographic mask defect and similar defect after repair by photodeposition. Defects are shown (a) in reflection, and (b) in transmission.

Fig. II-6. Al concentration vs depth, obtained from SIMS, for laser photochemically doped Si.



An important aspect of mask correction is that the repair be of sufficient durability to withstand the mechanical and chemical environment encountered in normal mask usage. The films which were obtained in our experiments were scrubbed with "Q-tips" in alcohol, acetone, and water rinses without damage. In addition they remained adherent to the substrate after contact with cellophane tape. Similarly durable depositions can be achieved with a pulsed UV laser if the laser intensity is carefully controlled.

D. J. Ehrlich    D. J. Silversmith  
T. F. Deutsch   R. M. Osgood, Jr.

#### D. SOLAR CELL FABRICATION BY LASER PHOTOCHEMICAL DOPING

We have recently demonstrated the use of both pulsed<sup>18</sup> and CW<sup>19</sup> UV lasers to dope localized regions in InP in order to produce ohmic contacts. In the pulsed case, the UV laser serves both to produce dopant atoms by dissociating a parent molecule and to simultaneously heat the substrate in order to produce an alloyed junction. We have now used a pulsed excimer laser to introduce p dopants into single-crystal n-Si substrates in order to form p-n junctions. We have been able to make Si solar cells with areas of several square millimeters by scanning techniques.

The UV source was a pulsed 193-nm ArF excimer laser operating at 5 Hz. Samples of n-Si, 2 to 5 ohm-cm resistivity, were enclosed in a 1-cm-long stainless steel cell, and the UV beam was focused on them with a BaF<sub>2</sub> lens. The beam size at the substrate was 1- × 3.7-mm and the peak fluence was ~0.2 J/cm<sup>2</sup>. Al or B dopant atoms were obtained by the dissociation of Al(CH<sub>3</sub>)<sub>3</sub> or B(CH<sub>3</sub>)<sub>3</sub> donor gases, with typical pressures of 5 or 10 Torr, respectively. The cell was translated through the beam at a rate of 3 to 6 mm/min., resulting in the formation of a p-doped region several millimeters in length.

The p-n junctions thus formed functioned as solar cells. Open-circuit voltages of 0.50 V were obtained for both Al and B doping. The solar cell efficiency of the best devices is currently being evaluated.

Both B- and Al-doped samples were examined using secondary ion mass spectrometry (SIMS) performed at an outside laboratory. Measurements of B, Al, and C concentrations versus depth were obtained using a 5.5-keV 90% O<sub>2</sub><sup>+</sup>, 10% O<sup>+</sup> beam to sputter off 700-μm-square regions. B<sup>+</sup>- and Al<sup>+</sup>-implanted Si samples were used as calibration standards. Aluminum concentrations of 0.5 to 4 × 10<sup>19</sup> cm<sup>-3</sup> were obtained at the surface. Figure II-6 shows a concentration vs depth profile obtained from the SIMS data. The estimated junction depth, obtained by extrapolating the Al concentration vs depth curve to the 2 × 10<sup>15</sup> cm<sup>-3</sup> level corresponding to the substrate doping, is 0.12 μm. This depth range agrees well with the value 0.15 μm obtained using a mechanical grooving and staining technique. In addition, it indicates that the laser technique can produce the shallow junctions needed for solar cells.

The profiles of B-doped junctions showed several differences from those of Al-doped units. The junction depths, estimated from the SIMS data, ranged from 0.6 to 1 μm. The B concentration at the surface was 2 to 7 × 10<sup>21</sup> cm<sup>-3</sup>. The higher B concentration in part reflects the fact that the solid solubility of B in Si, 6 × 10<sup>20</sup> cm<sup>-3</sup>, is about one decade higher than that of Al. It also indicates a doping level in excess of the equilibrium solid solubility.

The results indicate that the laser photochemical doping technique can be used as a simple device fabrication technique. It can be used to produce shallow, abrupt p-n junctions; furthermore, it can be used to dope with materials, such as B, that are difficult to deposit by conventional evaporation techniques.

T. F. Deutsch    D. J. Ehrlich  
J. C. C. Fan    R. M. Osgood, Jr.

## REFERENCES

1. Solid State Research Report, Lincoln Laboratory, M.I.T. (1979:3), p.9.
2. Solid State Research Report, Lincoln Laboratory, M.I.T. (1974:4), p.23, DDC AD-A004763/9.
3. R.R. Patty, G.M. Russwurm, W.A. McClenny, and D.R. Morgan, Appl. Opt. 13, 2850 (1974).
4. E. R. Murray and J. E. van der Laan, Appl. Opt. 17, 814 (1978).
5. R. Reisfeld and C.K. Jorgensen, Lasers and Excited States of Rare Earths, (Springer-Verlag, Berlin, 1977); K.H. Yang and J.A. DeLuca, Phys. Rev. B 17, 4246 (1978) and references cited therein; L.I. Devyatkov, P.M. Lozovskii, V.V. Mikhailin et al., JETP Lett. 27, 576 (1978); V.V. Mikhailin, S.P. Chernov, and A.V. Shepelev, Sov. J. Quantum Electron. 8, 998 (1978).
6. D. J. Ehrlich, P. F. Moulton, and R. M. Osgood, Jr., Opt. Lett. 4, 184 (1979).
7. D. J. Ehrlich, P. F. Moulton, and R. M. Osgood, Jr., Paper Th. A4, OSA Topical Meeting on Excimer Lasers, Charleston, South Carolina, 11-13 September 1979.
8. G. Blasse and A. Bril, J. Chem. Phys. 47, 5139 (1967).
9. R.C. Ropp, J. Electrochem. Soc.: Solid State Sci. 115, 841 (1968).
10. R.R. Jacobs, W.F. Krupke, and M.J. Weber, Appl. Phys. Lett. 33, 410 (1978).
11. W. J. Miniscalco, J. M. Pellegrino, and W. M. Yen, J. Appl. Phys. 49, 12 (1978).
12. L. R. Elias, W. S. Heaps, and W. M. Yen, Phys. Rev. B 8, 4989 (1973).
13. K. H. Yang and J. A. DeLuca, Appl. Phys. Lett. 31, 594 (1977).
14. See for example, R. A. Kaplan, Solid State Technology, April 1976, pp. 74-78.
15. See for example, D. J. Silversmith and R. W. Mountain, Solid State Research Report, Lincoln Laboratory, M.I.T. (1979:3), pp. 45-47.
16. T. F. Deutsch, D. J. Ehrlich, and R. M. Osgood, Jr., Appl. Phys. Lett. 35, 175 (1979).
17. D. J. Ehrlich, T. F. Deutsch, and R. M. Osgood, Jr., Materials Research Symposium A, Cambridge, Massachusetts, 27-30 November 1979.
18. T. F. Deutsch, D. J. Ehrlich, R. M. Osgood, Jr., and Z. L. Liao, Appl. Phys. Lett. 36, 847 (1980).
19. D. J. Ehrlich, R. M. Osgood, Jr., and T. F. Deutsch, Appl. Phys. Lett. 36, 916 (1980).

### III. MATERIALS RESEARCH

#### THE CLEFT PROCESS, A TECHNIQUE FOR PRODUCING EPITAXIAL FILMS ON REUSABLE SUBSTRATES

A technique has been developed for using vapor-phase epitaxy (VPE) to prepare multiple single-crystal films of a semiconductor by a series of homoepitaxial growth runs on a single reusable substrate. After each successive run the upper surface of the grown film is bonded to a substrate of another material, and the film is then cleaved from the reusable substrate, leaving the latter ready for the next run. We have named this new technique the CLEFT process, an acronym for cleavage of lateral epitaxial films for transfer.

The development of the CLEFT process was motivated by the desire to reduce the cost and semiconductor material requirements of single-crystal GaAs solar cells. Conventional cells of this type incorporate not only a VPE-grown active region (less than 5  $\mu\text{m}$  thick) but also the growth substrate (250 to 400  $\mu\text{m}$  thick), which is cut from a melt-grown single-crystal ingot of GaAs (Refs. 1-3) or Ge (Ref. 4). If the active region can be grown on a reusable substrate, the quantity of single-crystal ingot material required for cell production will be drastically reduced, resulting in a marked reduction in cost.

The key element of the CLEFT process is the use of lateral VPE growth.<sup>5</sup> Our experiments have shown that if a mask with appropriately spaced stripe openings is deposited on a (110) GaAs substrate, the epitaxial growth initiated on the GaAs surface exposed through the openings will be followed by lateral growth over the mask, eventually producing a continuous single-crystal film that can be grown to any desired thickness. The upper surface of the film is then bonded to a secondary substrate of some other material. If there is poor adhesion between the mask material and the GaAs, the film will be strongly attached to the GaAs substrate only at the stripe openings. Since a weak plane has been created by the mask and because the (110) plane is the principal cleavage plane of GaAs, the film can be cleaved from the GaAs substrate without significant degradation of either.

The following procedure has been used in applying the CLEFT process to GaAs. Photoresist is applied to the polished surface of a (110)-oriented GaAs wafer, then patterned with 2.5- $\mu\text{m}$ -wide stripe openings on 50- $\mu\text{m}$  centers by standard photolithographic techniques, and thermally carbonized. The resulting mask configuration is shown schematically in Fig. III-1(a). A GaAs VPE film is grown on the masked substrate at 750°C by the  $\text{AsCl}_3\text{-Ga-H}_2$  method in the growth system previously described.<sup>4</sup> Figures III-1(b) and -1(c) show the film at two intermediate stages of growth: just after it has begun to grow laterally over the mask and shortly before it becomes continuous. Under the growth conditions used, the ratio of lateral to vertical growth rates is about 25, so that the film becomes continuous when it is only about 1  $\mu\text{m}$  thick, as shown in Fig. III-1(d). Growth is continued until the thickness reaches 5 to 10  $\mu\text{m}$ . The final film obtained is quite uniform in thickness, and in some instances it has been as smooth as an epilayer grown directly on an unmasked substrate.

The technique used for separating the GaAs film from its GaAs substrate is illustrated by the schematic diagram shown in Fig. III-2. The upper surface of the film is bonded with epoxy to a glass secondary substrate about 0.25 mm thick. The GaAs and glass substrates are then bonded with wax to glass plates about 5 mm thick that serve as cleaving supports. A metal wedge is inserted between the two glass plates and tapped gently with a hammer, causing the



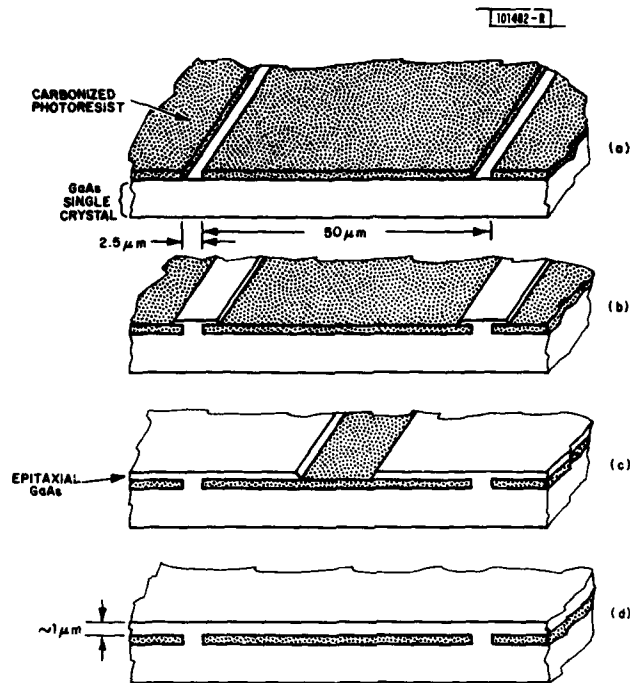


Fig. III-1. Schematic diagram showing formation of GaAs film by lateral epitaxial overgrowth. In (a) the single-crystal substrate is shown before growth begins. The sequence (b)-(d) shows how the GaAs grows together laterally from the stripe openings to form a single-crystal film.

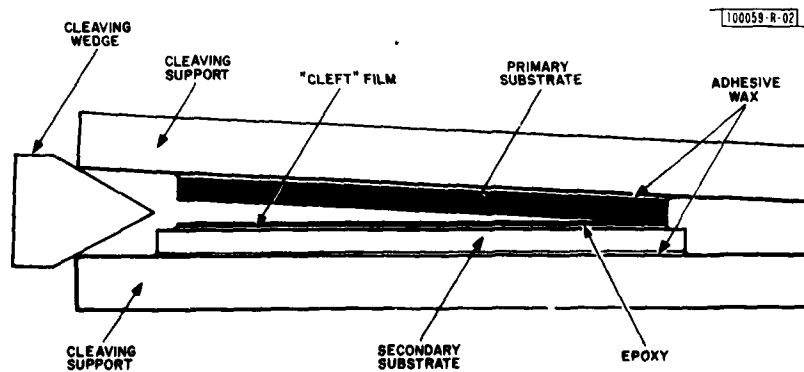


Fig. III-2. Cross-sectional view of an epitaxial film being transferred to a substrate. This is the last step in the CLEFT process.

GaAs film to be cleaved from the GaAs substrate but leaving it mounted on the glass substrate. Finally, the GaAs primary substrate is removed from its glass cleaving support plate and cleaned to remove any photoresist residue remaining after the cleaving step, making the substrate ready for another cycle of the CLEFT process.

As a demonstration that the CLEFT process can be used to prepare multiple GaAs films, we have carried out four CLEFT cycles with the same single-crystal GaAs substrate. In Fig. III-3 are photographs showing the four successive films obtained, along with the GaAs substrate after removal of the last film. All five surfaces are of high quality except for that of the first film, which was damaged over some of its area during cleaving because of the presence of bubbles in the epoxy layer used to bond it to the glass substrate. The film thicknesses are 5, 10, 10, and 8  $\mu\text{m}$ , respectively. The area of each film, about 4  $\text{cm}^2$ , is slightly less than the substrate

Fig. III-3. Four laterally overgrown epitaxial films which were cleaved and transferred from one single-crystal substrate by the CLEFT process.

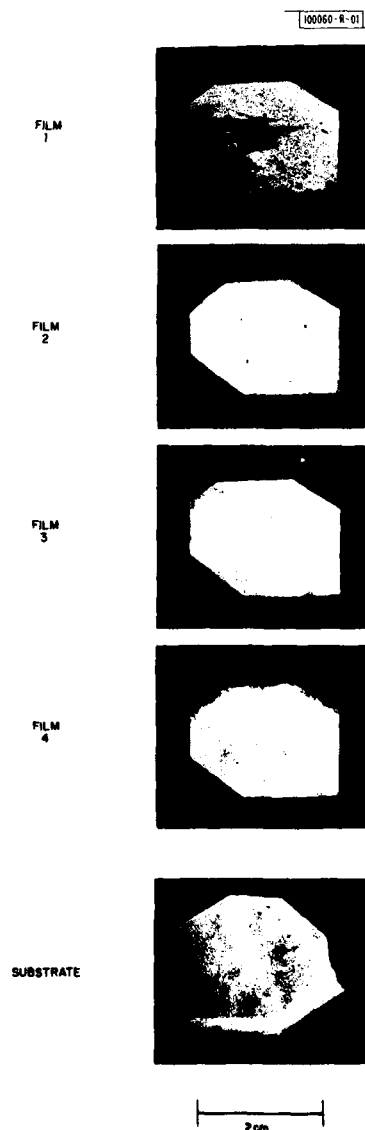


TABLE III-1 ELECTRICAL PROPERTIES OF EPITAXIAL FILMS					
Sample	Thickness ( $\mu\text{m}$ )	Temperature (K)	Electron Density ( $\text{e}/\text{cm}^3$ )	Electron Mobility ( $\text{cm}^2/\text{V}\text{-sec}$ )	$N_A/N_D$
Epitaxial film on semi-insulating substrate	9.4	300	$3.3 \times 10^{16}$	5,900	0.31
		77	$2.6 \times 10^{16}$	11,100	
Lateral epitaxial film over carbonized photoresist on semi-insulating substrate	5.8	300	$3.6 \times 10^{16}$	4,900	-
		77	-	-	
	5.8	300	$3.5 \times 10^{16}$	4,800	0.42
		77	$2.7 \times 10^{16}$	9,100	

area because the stripe openings in the photoresist mask were not extended to the edge of the substrate, in order to avoid problems associated with photoresist edge buildup.

An additional experiment was performed in order to obtain an initial evaluation of the electrical properties of GaAs films prepared by the CLEFT process. In a single VPE run, S-doped films were grown on two Cr-doped, semi-insulating (110) GaAs substrates, one masked with carbonized photoresist for the CLEFT process and the other an unmasked control sample for conventional growth. Both samples were cut into 0.5-cm squares, ohmic contacts were made to the corners, and Hall and resistivity measurements were made by the van der Pauw technique. Without removing the contacts and lead wires, the CLEFT film grown on the masked substrate was bonded to a glass substrate and cleaved from the GaAs substrate. The electrical measurements were then repeated. Measurements were made at both 300 and 77 K on the conventional film and on the CLEFT film after cleavage, but only at 300 K on the as-grown CLEFT film. Table III-1 gives the carrier concentration and Hall mobility values determined from the electrical data. There is no significant difference between the results obtained at 300 K for the CLEFT film before and after transfer, showing that bonding to the glass substrate and cleavage from the GaAs substrate did not result in film degradation. Both the CLEFT and conventional films are n-type, with essentially the same carrier concentration. The conventional film has an electron mobility which is near the maximum possible for its carrier concentration. The mobility of the CLEFT film is somewhat lower than that of the conventional film, but the ratio of acceptor to donor concentration ( $N_A/N_D$ ) is still only 0.4 for the CLEFT film.

There do not appear to be any intrinsic features of the CLEFT process that set an upper limit either on the number of films that can be grown on a single substrate or on the area of the individual films. Using masks with appropriately spaced openings should permit the growth and transfer of films as thin as 0.5  $\mu\text{m}$  with any desired geometry, and it should be possible to use a wide variety of secondary substrates, including both amorphous and crystalline materials. Furthermore, we believe that there is a high probability of using the CLEFT process for semiconductors other than GaAs, and we have initiated the development of techniques for its application to Si and InP. Because it can greatly reduce the quantity of bulk single-crystal materials now being used in the fabrication of semiconductor devices utilizing thin active regions, the CLEFT process should permit a drastic reduction in the cost of devices such as solar cells where wafer cost is currently a major factor. Because it can be used to obtain high-quality single-crystal films on a variety of secondary substrates, the process can provide new approaches to the fabrication of integrated circuits on insulating substrates and multi-layer devices and circuits. Therefore we believe that the CLEFT process has the potential for being a significant development in semiconductor technology.

R.W. McClelland  
C.O. Bozler  
J.C.C. Fan

#### REFERENCES

1. H. J. Hovel and J. M. Woodall, J. Electrochem. Soc. 120, 1246 (1973).
2. C. O. Bozler and J. C. C. Fan, Appl. Phys. Lett. 31, 629 (1977).
3. J. C. C. Fan, C. O. Bozler, and R. L. Chapman, Appl. Phys. Lett. 32, 390 (1978).
4. C. O. Bozler, J. C. C. Fan, and R. W. McClelland, 7th International Symp. on Gallium Arsenide and Related Compounds, St. Louis, 1978 (The Institute of Physics, London, 1979), p. 429.
5. F. W. Tausch, Jr. and A. G. Lapierre, III, J. Electrochem. Soc. 112, 707 (1965).

#### IV. MICROELECTRONICS

##### A. CHARGE-COUPLED DEVICES: SAW/MOSFET MEMORY CORRELATOR

An earlier report<sup>1</sup> described a CCD-programmable SAW matched filter in which the filter function is controlled by the charge pattern clocked into the CCD. We have used this device to demonstrate a new kind of memory correlator which does not require the CCD portion of the semiconductor chip, but enters an RF reference waveform on the SAW input port. A schematic diagram of this new device is shown in Fig. IV-1. The sampling structure consists of 300 MOSFETs which record an image of the reference waveform on the sampling fingers.

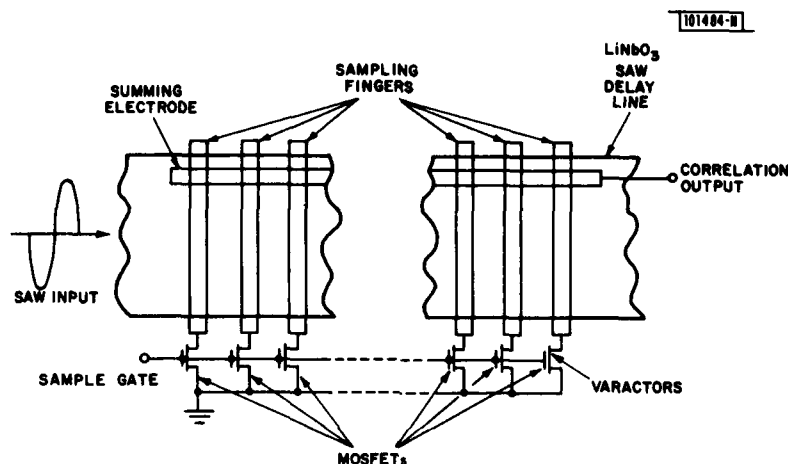


Fig. IV-1. Schematic diagram of the SAW/MOSFET memory correlator.

The low on-resistance of the MOSFETs allows piezoelectric displacement currents to flow between the sampling fingers. This current flow causes an exchange of charge between the fingers so that the charge pattern on the fingers corresponds to the instantaneous amplitude of the SAW. If the sampling transistors are suddenly turned off, this exchange is stopped, and a replica of the SAW waveform is stored as a charge pattern on the fingers.

The sequence of device operation is as follows. With the MOSFETs turned on a SAW reference is launched. When the reference pattern is aligned with the coupling fingers, the transistors are turned off with a rapid (3 nsec) fall time. This operation biases each of the fingers with a local sample of the SAW waveform. A subsequent SAW signal is multiplied by this sampled reference through a set of varactors formed by the drain regions of the MOSFETs, and the products are summed on the output electrode in the same way as for the CCD-programmable matched filter.<sup>1</sup>

Figure IV-2 is an example of the correlator output waveform at a carrier frequency of 100 MHz. The input is a 1.8- $\mu$ sec-long rectangular reference pulse (a single code bit) followed by an identical signal pulse, both at an input lower level of 27 dBm. The peak of the triangular output envelope shown in Fig. IV-2 is at a power level of about -46 dBm at 100 MHz, or about

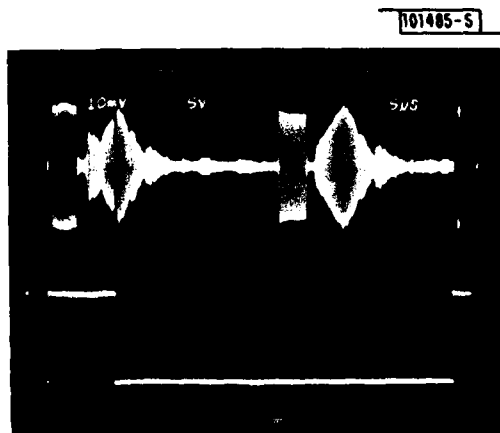


Fig. IV-2. Oscilloscope of correlator operation at 100 MHz. Top: output waveform; bottom: sampling waveform.

5 dB worse than the CCD-programmable filter. The rectangular pulses on the output waveform are caused by direct feedthrough of the input waveform to the summing electrode. This unwanted signal can be reduced to an insignificant level by introducing sufficient physical separation between the input transducer and the output electrode.

This experiment demonstrates the feasibility of using a simple array of MOSFETs and coupling fingers to realize an acoustoelectric memory correlator. The main feature of this new device is its ability to perform memory correlation with a coupling structure which adequately samples the information bandwidth, but under-samples the SAW carrier.<sup>2</sup> Since GaAs is a piezoelectric semiconductor, this new mode of operation is attractive for use in a monolithic GaAs SAW/MOSFET memory correlator.

D.L. Smythe  
R.W. Ralston

#### B. CHARGE-COUPLED DEVICES: PROGRAMMABLE MATCHED FILTER

A modification of the 16-stage by 4-bit, digitally programmable CCD transversal-filter structure reported earlier<sup>3</sup> is described below. The original device used four, 16-stage by 1-bit filters with bit weighting and summation of the charge performed at the output of each filter section. However, certain design limitations of this approach make it difficult to achieve more stages or more bits per tap while retaining a reasonable chip area and input-output pin count. The new architecture results in a much simpler chip design, and a 32-stage, CCD transversal-filter with taps programmable as 6-bit digital words has been built. Matched filtering using a chirp waveform has been demonstrated.

A key component of the new filter is a high-speed, multiplying D/A converter (MDAC) which is illustrated in Fig. IV-3(a). The data bits control the charge flow into the CCD input gates and thereby perform a multiplication of the charge under these gates by 0 or 1. The details of this process have been described previously.<sup>4,5</sup> The area of the gate corresponding to bit  $N$  is proportional to  $2^{N-1}$ , and the quantity of charge transferred by the gate is then proportional to the product of the value of bit  $N$ , the gate area, and the analog signal. The device is designed to use tap weights expressed in 2's complement format which requires that bit 6, the most significant bit (MSB), be handled separately from the five remaining bits. In the current design the MSB is applied to a gate of area  $32A$ , and the charge is carried in a separate delay line to the

charge detection circuit. The output signals from the two delay lines are subtracted, and the output signal then represents the product of the analog signal and the digital word.

The transversal filter structure shown in Fig. IV-3(b) consists of two banks of 32 delay lines with the length of the lines increasing from 1 to 32 stages. The control logic circuitry

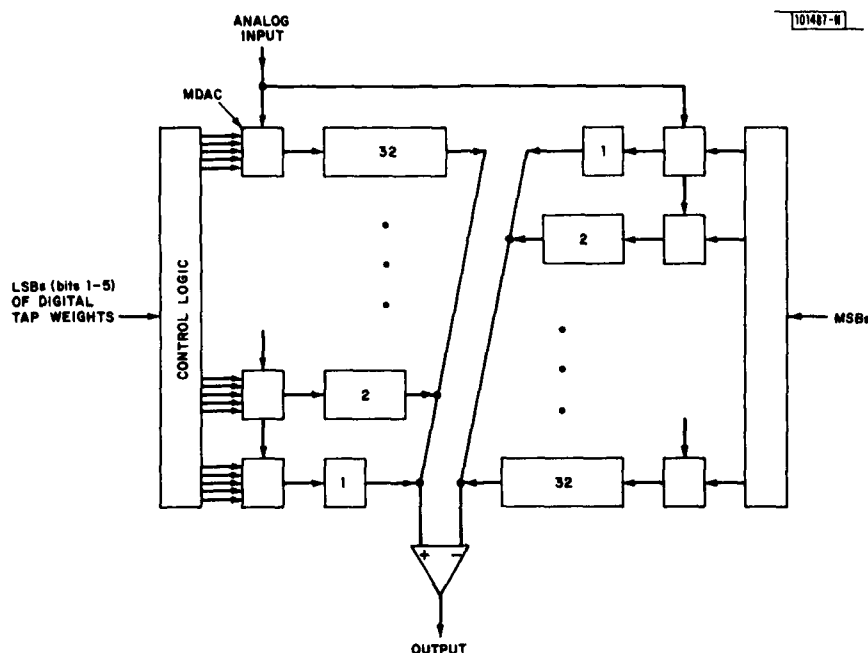


Fig. IV-3. (a) Schematic of the CCD multiplying D/A converter.

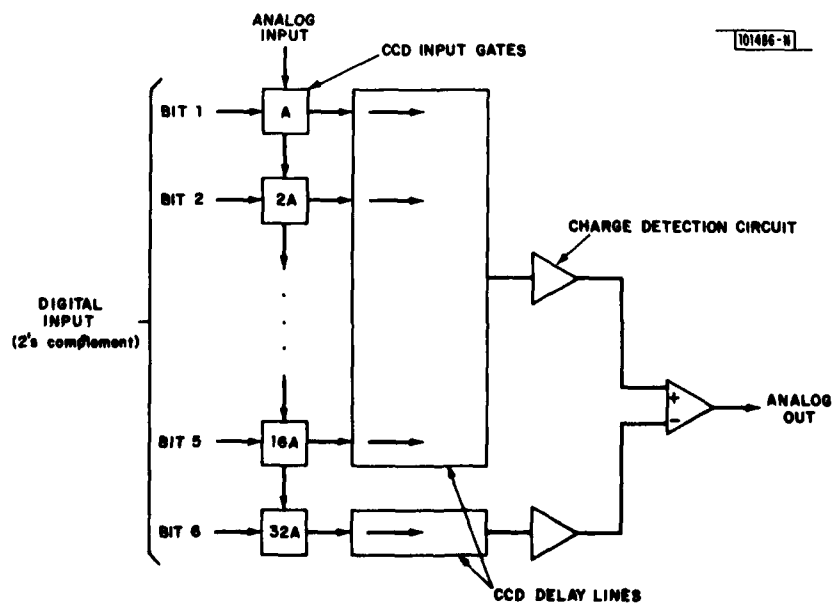


Fig. IV-3. (b) Schematic of the 6-bit, 32-stage CCD programmable transversal filter incorporating MDACs at the delay-line inputs.



combines shift registers which serially load the tap weight values and a set of latches into which these data are parallel-transferred to provide the inputs to the MDACs. An MDAC is located at the input to each delay line, with the MDACs in the left-hand portion of Fig.IV-3(b) consisting of the first 5 of the 6 bits and those on the right-hand portion of Fig.IV-3(b) the 6th or MSB bit. The digital input to each MDAC represents one of the 32 tap weight values. The charge packets are clocked along the delay lines and summed on one of the two common charge collection lines along the delay-line outputs. The outputs of the two sections are then subtracted in an off-chip differential amplifier to form the output signal.

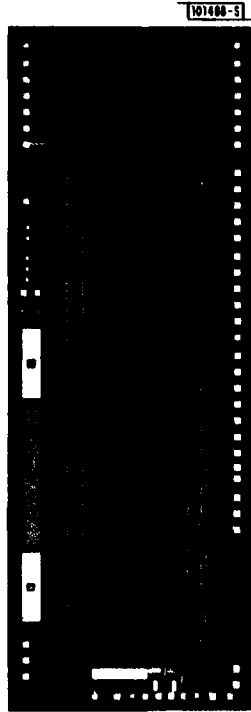


Fig. IV-4. Photograph of 6-bit, 32-tap, digitally programmable CCD transversal filter.

A photomicrograph of the 6-bit, 32-stage device is shown in Fig.IV-4. The chip size is 8.4 mm  $\times$  2.8 mm. The device performance as a matched filter has been demonstrated for the case of a chirp waveform where the tap weights of the device are programmed as a cosine down-chirp, i.e.,

$$h_n = \cos 16\pi \left( \frac{31-n}{32} \right)^2 \quad n = 0, 1, \dots, 31$$

and the numbers,  $h$ , are digitized to 6-bit accuracy. The impulse response of the device is shown in Fig.IV-5. When a cosine up-chirp

$$V_{in}(m) = \cos 16\pi \left( \frac{m}{32} \right)^2 \quad m = 0, 1, \dots, 31$$

is continuously applied to the CCD input [top trace in Fig.IV-6(a)], the output of this filter [the lower trace in Fig.IV-6(a)] contains the expected correlation spike. The test was performed -

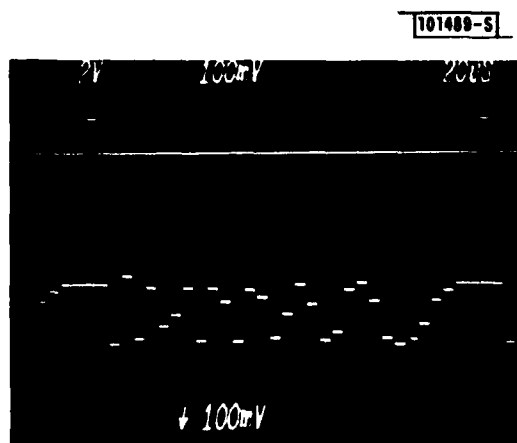


Fig. IV-5. Impulse response of the 6-bit, 32-tap filter when the tap weights are programmed as a cosine chirp waveform.

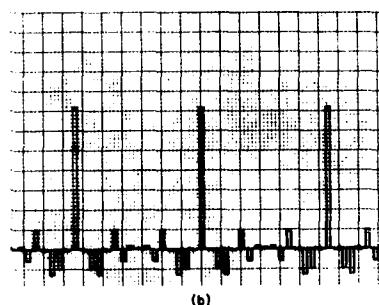
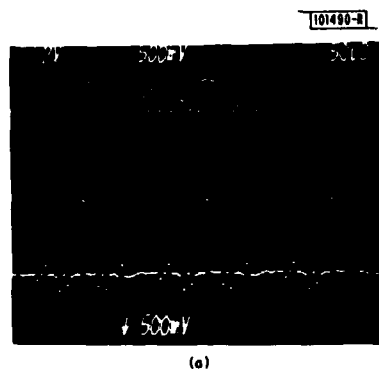


Fig. IV-6. (a) Top trace: a repeated cosine chirp waveform input signal. Bottom trace: correlation output of the filter when the taps are programmed as in Fig. IV-5. (b) Calculated filter output for the same conditions.

using a probe card, and this limited the clock frequency to 200 kHz. The calculated output shown in Fig. IV-6(b) shows good agreement with the measured waveform, although additional evaluation will be needed to quantify the tap-weight accuracy.

A. M. Ch'ang  
B. E. Burke

#### C. X-RAY LITHOGRAPHY AT $\sim 100 \text{ \AA}$ LINEWIDTHS USING X-RAY MASKS FABRICATED BY SHADOWING TECHNIQUES.

A new technique for fabricating high-contrast, x-ray masks with precisely controlled linewidths smaller than  $100 \text{ \AA}$  has been developed.<sup>6,7</sup> The technique is based on the deposition at an oblique angle ("shadowing") of x-ray absorber material onto relief structures of triangular and square section in a polyimide membrane. The success of the technique depends on the perfection of the relief structures. Extremely smooth and reproducible triangular-cross-section surface relief structures can be fabricated in single-crystal silicon by anisotropic chemical etching,<sup>8</sup> and square-cross-section surface relief structures with smooth vertical sidewalls and sharp corners can be fabricated in silicon dioxide by reactive ion etching in  $\text{CHF}_3$  gas.<sup>9</sup> These structures can then be transferred to a thin polyimide plastic membrane by molding. In the case of the triangular cross section, the linewidth of the final pattern is precisely determined by the

shadowing angle. For the square cross section, the thickness of the absorber material on the vertical sidewall determines the linewidth.

The procedure for fabricating an x-ray mask using a triangular surface relief structure in silicon is shown in Fig. IV-7. The relief structure in the silicon surface, which is fabricated by anisotropic etching in KOH through an  $\text{Si}_3\text{N}_4$  mask, is covered with a liquid polyimide plastic<sup>10</sup> as shown in Fig. IV-7(a). The plastic is polymerized by heating and removed from the silicon mold by peeling after very brief immersion in diluted HF or by etching away the substrate in 96% HF, 4%  $\text{HNO}_3$ . The polyimide-membrane surface-relief structure is then mounted on a metal or plastic ring and shadowed with an x-ray absorber material as shown in Fig. IV-7(c). The linewidth of the projection of the x-ray absorber pattern can be varied by choosing the shadowing angle.

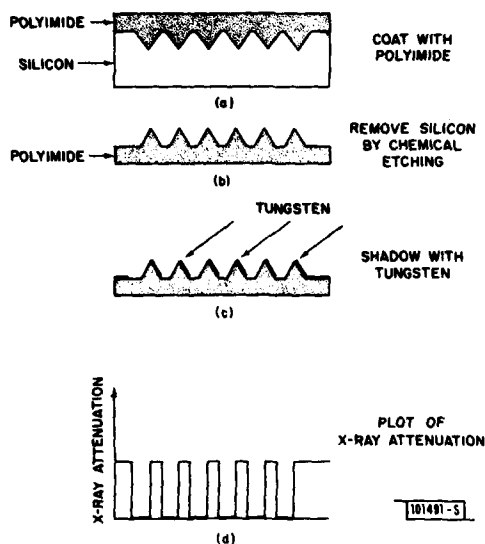


Fig. IV-7. Fabrication procedure for shadowed triangular-profile polyimide membrane x-ray mask and the resulting carbon x-ray attenuation. The x-ray mask linewidth can be varied by varying the shadowing angle.

A 1- $\mu\text{m}$ -period, triangular-profile relief structure in a 1- $\mu\text{m}$ -thick polyimide membrane was made by the process depicted in Fig. IV-7. One area of this structure was shadowed at  $19^\circ$  with 200 Å of tungsten, another area was shadowed at  $33^\circ$  with 200 Å of tungsten, and a third area was shadowed from both sides at  $33^\circ$ . The resulting mask was then replicated in PMMA using carbon K x rays. The mask and substrate were held in intimate contact during replication. The resulting 1500, 3500, and 7000 Å linewidth structures are shown in Fig. IV-8. The linewidths obtained agree closely with the calculated values.

For linewidths smaller than 400 Å, it is more appropriate to fabricate the x-ray mask by shadowing a square-wave-cross-section relief structure. This mask fabrication procedure is illustrated in Fig. IV-9. A square-wave surface relief structure is first fabricated in  $\text{SiO}_2$  by methods described in an earlier paper.<sup>9</sup> A polyimide replica of the structure is shadowed at an angle, yielding the mask structure shown in Fig. IV-9(c). The relative x-ray attenuation of the wide and narrow regions can be such that by overexposure and/or overdevelopment only the narrow high-contrast region of the mask will be replicated in PMMA. A 3200-Å-period, square-wave structure was made in polyimide by the process shown in Fig. IV-9 and shadowed at an

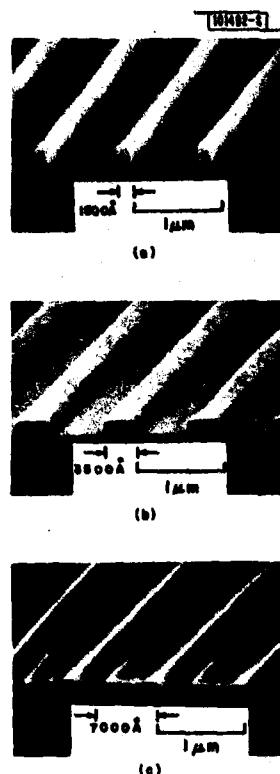


Fig. IV-8. SEM micrograph of 1- $\mu$ m-period PMMA gratings on amorphous  $\text{SiO}_2$  substrates produced by carbon K x-ray lithographic replication of 1- $\mu$ m-period triangular-profile polyimide masks shadowed with 200  $\text{\AA}$  of tungsten at (a)  $19^\circ$ , (b)  $33^\circ$ , and (c) both sides at  $33^\circ$ .

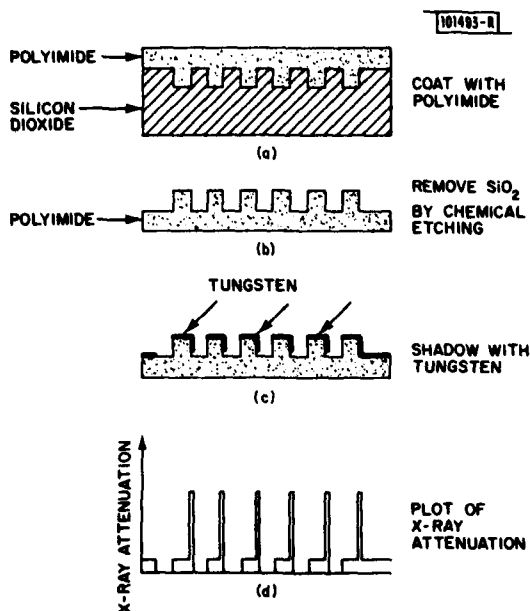


Fig. IV-9. Sequence of steps for fabricating a shadowed square-wave-profile polyimide x-ray mask. The  $\text{SiO}_2$  square-wave structure is made by reactive ion etching with  $\text{CHF}_3$  through a chromium mask.

angle of  $30^\circ$  with 200  $\text{\AA}$  of tungsten, yielding a mask with a 180- $\text{\AA}$ -wide linewidth and 8 dB of contrast. This mask was replicated in 600- $\text{\AA}$ -thick PMMA using carbon K x rays. Figure IV-10 shows a TEM micrograph of a 600- $\text{\AA}$ -high, 200- $\text{\AA}$ -wide line which resulted from the exposure. To make the micrograph, a tungsten-shadowed carbon replica was made of the relief structure exposed in the PMMA. Also shown is a perspective view of the structure as determined from the micrograph.

Because extremely smooth vertical sidewalls can be obtained in square-wave relief structures, masks with linewidths smaller than 100  $\text{\AA}$  can be made. By shadowing such structures alternately with tungsten and an x-ray transparent material such as carbon, high-contrast x-ray masks with lines and spaces less than 100  $\text{\AA}$  in width can be made. Figure IV-11 shows a micrograph of a mask with lines as small as 20  $\text{\AA}$ . Such masks are ideally suited for investigating the ultimate resolution of x-ray lithography and for generating simple device geometries.

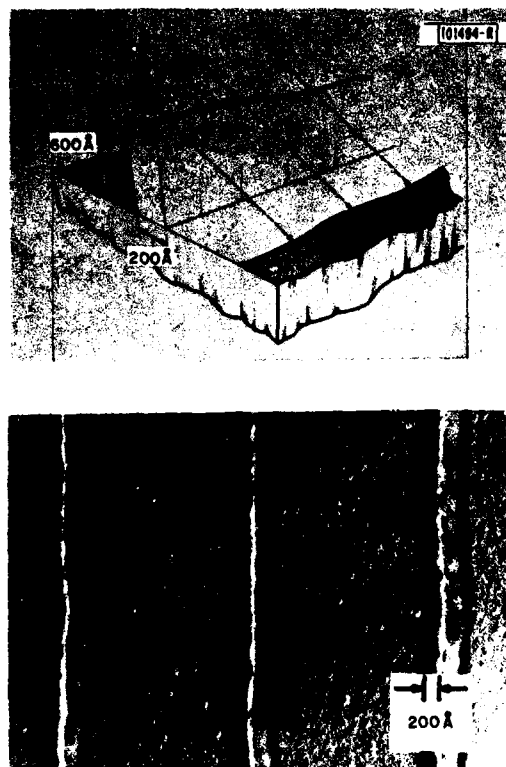
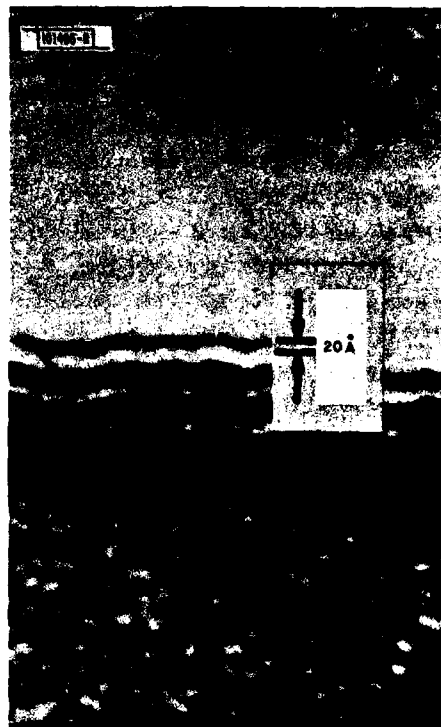


Fig. IV-10. Transmission electron micrograph of a tungsten-shadowed carbon replica of a 200 Å-linewidth 600 Å-high PMMA structure exposed with the carbon K x ray on a thick SiO<sub>2</sub> substrate using a 3200 Å period shadowed square-wave polyimide membrane x-ray mask. The perspective view of the original PMMA structure shown was deduced from the micrograph of the carbon replica.

Fig. IV-11. Transmission electron micrograph of an x-ray mask fabricated by the shadowing technique, demonstrating the extremely narrow linewidths that can be obtained. Five nearly opaque tungsten lines are separated by four transparent carbon spurs. The tungsten is 300 Å thick and the narrowest line is about 20 Å wide.



Using a multiple-shadowed square-wave mask, 175 Å lines and spaces have been replicated in PMMA with carbon K x rays.<sup>7</sup>

D.C. Flanders

#### D. SUBMICROMETER-GATE-LENGTH GaAs FET

GaAs FETs with gate lengths of less than 0.5 μm are currently of interest for operation as low-noise amplifiers in the 20- to 40-GHz frequency range. The fabrication of these small gates is beyond the capability of conventional optical lithographic systems, and other forms of lithography must be utilized. Electron beams and soft x rays are capable of exposing features in resist with dimensions of 250 Å and below.<sup>11,12</sup> However, even though submicrometer technology has produced structures much smaller than those required for the gates of 40-GHz FETs, the techniques are not readily usable in normal processing sequences for fabricating semiconductor devices. The present report describes a submicrometer-gate-length GaAs FET which was fabricated as a test vehicle for the development of a device processing sequence which would not require alignment when writing or replicating the submicrometer patterns. Submicrometer alignment is eliminated by having the gate processing step precede the ohmic contact step, in reverse order from the conventional approach,<sup>13</sup> and an additional benefit is achieved in that the fabrication yield is higher due to the planar surface of the wafer. Elimination of the need for alignment enables the use of either direct electron-beam writing of the gates on the wafer as described below, or replicating a submicrometer-gate mask onto the wafer by x-ray lithography in systems with no alignment capability.

The starting material for these devices is a chromium-doped semi-insulating GaAs substrate with a buffer layer that is epitaxially grown in a vapor-phase reactor. The buffer layer is then implanted with selenium ions to produce an electron concentration of  $10^{17} \text{ cm}^{-3}$ . Subsequently the wafer is coated with a layer of  $\text{Si}_3\text{N}_4$  deposited by plasma CVD and 3500 Å of PMMA. Next, gate patterns of 0.3  $\mu\text{m}$  are written using scanning electron beam lithography, and the patterns are dry etched into the  $\text{Si}_3\text{N}_4$  layer in a barrel-type plasma reactor. A thin aluminum film is then evaporated onto the wafer and the metal gates are formed by lifting off the excess aluminum when the remaining PMMA is dissolved. It is essential in the fabrication of the gates that neither the deposition of  $\text{Si}_3\text{N}_4$  nor the subsequent dry-etch introduces damage to the underlying GaAs layer. That this is the case is confirmed by the low (1.05) n-factor of diodes fabricated following the above sequence, as shown in Fig. IV-12. During the dry-etching of the silicon nitride layer, there is erosion of the resist mask. Consequently, the resulting gates are 0.45  $\mu\text{m}$  long, approximately 1500 Å wider than the original pattern on PMMA. Further work on the optimization of relative thicknesses of PMMA and silicon nitride is necessary to achieve more accurate control of dimensions.

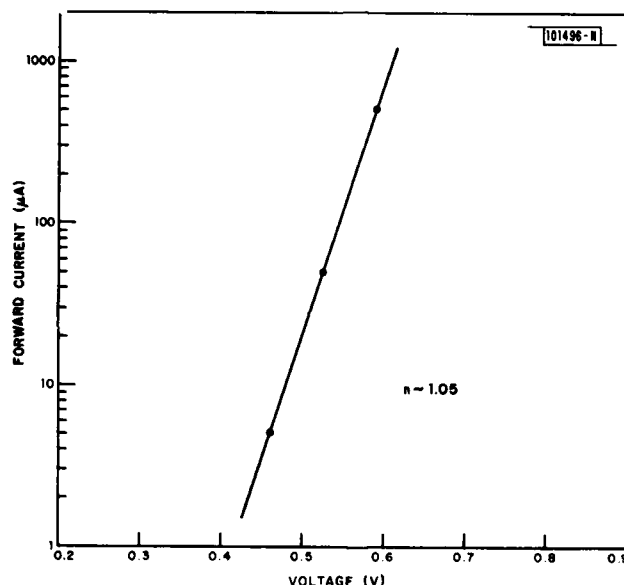


Fig. IV-12. I-V curve of plasma-etched  $\text{Si}_3\text{N}_4$  Schottky-barrier diodes.

After the submicrometer gates are fabricated, ohmic contacts are aligned optically to the gates. The minimum gate-source spacing is limited to  $\sim 1.5 \mu\text{m}$  by the optical realignment accuracy. The ohmic contacts are based on a Au-Ge system capable of achieving contact resistivities in the  $10^{-6} \text{ ohm-cm}^2$  range. Finally, the devices are isolated by means of high energy proton bombardment. The fabrication yields are typically in excess of 75%. The high yield figure reflects the conservative approach taken in the choice of the thin gate metal and the realignment of the drain and source contacts to the gate.

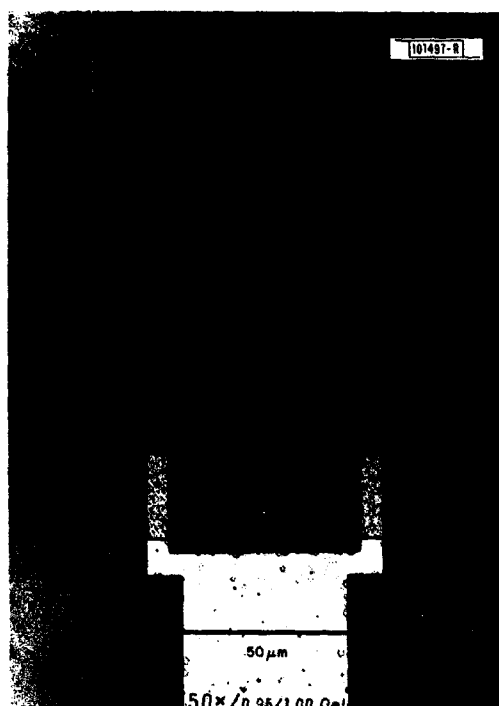


Fig. IV-13. Photograph of a submicrometer-gate-length GaAs FET. Total gate dimensions are  $0.45 \mu\text{m} \times 104 \mu\text{m}$ .

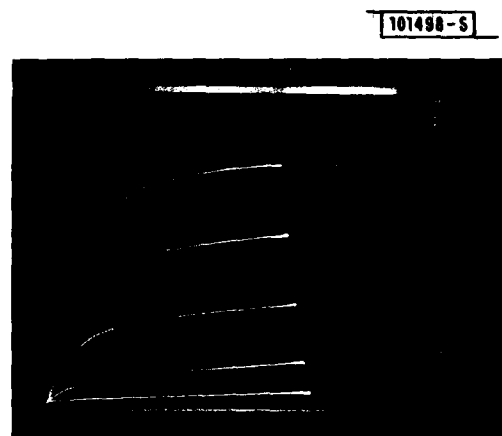


Fig. IV-14. DC characteristics of submicrometer FET.

A test FET is shown in Fig. IV-13. The device consists of two  $0.45\text{-}\mu\text{m}$  by  $52\text{-}\mu\text{m}$  gates in a drain-source spacing of  $4 \mu\text{m}$ . The drain characteristics of a typical device from which the DC parameters are obtained are shown in Fig. IV-14. The FET exhibits a saturation current of  $15.2 \text{ mA}$ , a transconductance of  $9.6 \text{ mmho}$ , and a pinch-off voltage of  $2.2 \text{ V}$ . In RF measurements, the devices typically exhibit a noise figure of  $3.5 \text{ dB}$  at  $12 \text{ GHz}$  with an associated gain of  $5 \text{ dB}$ . At  $18 \text{ GHz}$ , the FETs had  $6 \text{ dB}$  of gain. A plot of the maximum available gain vs frequency is shown in Fig. IV-15. The primary reason for the limited performance of this device is the high gate resistance associated with the thin gate metallization. It is apparent from the high device fabrication yields that the metal thickness can be increased without degrading the yield figure significantly. In future wafer processing runs, increases in gate metal thickness and other modifications will be interweaved with improvements in fabrication techniques to insure proper balance between the upgrading of device performance and the resulting fabrication yield.

A. Chu	G. Lincoln
A. Gopinath*	M. Pierce
G. Durant	C. Smith

\* Group 33



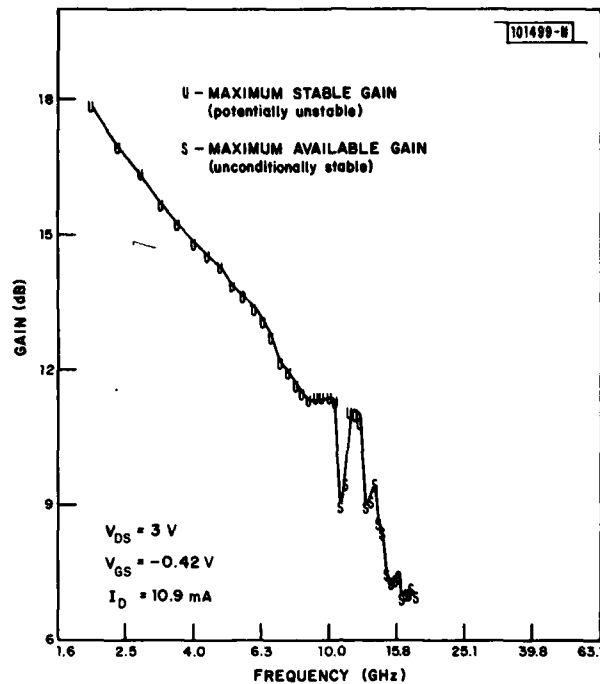


Fig. IV-15. Maximum available gain vs frequency for a typical submicrometer FET.

#### REFERENCES

1. Solid State Research Report, Lincoln Laboratory, M.I.T. (1979:2), pp.51-54, DDC AD-A078676.
2. *Ibid.* (1977:4), pp.37-39, DDC AD-A052463/7.
3. A.M. Chiang, B.E. Burke, D.L. Smythe, D.J. Silversmith, and R.W. Mountain, Proc. 5th International Conf. on CCDs, Edinburgh 1979, pp.230-236.
4. Solid State Research Report, Lincoln Laboratory, M.I.T. (1980:1), pp.33-35.
5. *Ibid.* (1977:4), pp.29-31, DDC AD-A041226/2.
6. D.C. Flanders, J. Vac. Sci. Technol. **16**, 1616 (1979).
7. D.C. Flanders, Appl. Phys. Lett. **36**, 93 (1980).
8. Kenneth E. Bean, IEEE Trans. Electron. Devices **ED-25**, 1185 (1978).
9. D.C. Flanders, Henry I. Smith, H.W. Lehmann, R. Widmer, and D.C. Shaver, Appl. Phys. Lett. **32**, 112 (1978).
10. D.C. Flanders and Henry I. Smith, J. Vac. Sci. Technol. **15**, 995 (1978).
11. W.W. Molzen, A.N. Broers, J.J. Cuomo, J.M.E. Jarper, and R.B. Laibowitz, J. Vac. Sci. Technol. **16(2)**, 269 (1979).
12. D.C. Flanders, J. Vac. Sci. Technol., **16(6)**, 1615 (1979).
13. T.G. Blocker, H.M. Mackessey, and F.H. Doerbeck, J. Vac. Sci. Technol. **15(3)**, 965 (1978).

## V. ANALOG DEVICE TECHNOLOGY

### A. APPLICATION OF A SAW CHIRP SPECTRUM ANALYZER TO AN INFRARED DOPPLER RADAR

#### 1. Introduction

Lincoln Laboratory has been conducting an analytical and experimental study of an Infrared Airborne Radar (IRAR) for a near-all-weather air-to-ground tactical mission.<sup>1,2</sup> The radar uses a pulsed CO<sub>2</sub> laser operating at 10.6- $\mu$ m wavelength to provide high-resolution images of ground objects which would be classified and identified by an operator. In the operational sequence, prior to imaging, the radar detects moving objects by using the same CO<sub>2</sub> laser in a CW mode. The Doppler effect of moving objects is used to discriminate them from the laser signal returned from the ground. This concept is the same as a moving target indicator (MTI) for a conventional microwave radar; however, important details are different as a consequence of the high frequency (30,000 GHz) of the radar.

The resolution and bandwidth requirements of a spectrum analyzer needed for the detection or acquisition mode of the infrared radar are well matched to the parameters easily available from a surface-acoustic-wave (SAW) chirp-transform spectrum analyzer system.<sup>3</sup> Furthermore, the size, weight, and power advantages of the SAW approach are particularly important for this airborne tactical application. For these reasons, an analysis has been conducted of the signal processing trade-offs for a Doppler acquisition system and a breadboard SAW chirp-spectrum analyzer has been constructed and installed with IRAR demonstration equipment in a laboratory van. This report summarizes the analysis and describes the equipment that was installed. A subsequent report will describe results of acquisition experiments.

#### 2. Infrared Radar

A block diagram of the infrared laser radar showing the SAW chirp-transform processor is shown in Fig.V-1.

The high frequency (and thus short wavelength) of the infrared radar signal produces high spatial resolution, large Doppler shifts, and high path loss, all of which affect the signal processing requirements. These requirements are outlined below.

Because of the short wavelength, even a modest aperture gives a very narrow transmit and receive beam. Most targets are completely resolved, and thus the usual clutter-to-signal problem (called subclutter visibility) which dictates large dynamic range equipment and low Doppler sidelobes is not an issue for the infrared radar.

The small beam, however, must be scanned through a large angle ( $\pm 30^\circ$ ) and, because of the forward motion of aircraft, the scan rate is very high. In order to accommodate limitations of commercially available mirror mounts ( $\sim 1$  rad/sec scan rate) it was necessary to use 12 laser beams in parallel.<sup>2</sup> As a consequence, 12 sets of identical channels of signal processing equipment are required, thus tightening speed, size, weight, and power requirements.

The extremely high frequency of the infrared signal results in very large Doppler frequency shifts, with a 1-mph target having a shift of 84 kHz relative to a stationary target. A bandwidth of about 10 MHz is required to accommodate targets moving  $\pm 50$  mph.

An additional consequence of the infrared wavelength to signal processing is the attenuation caused by fog and smoke. The system has been designed to penetrate as much as 3 dB/km of

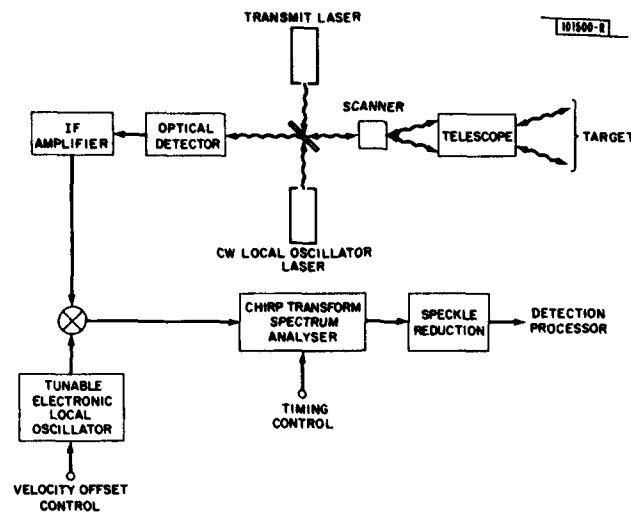


Fig. V-1. Infrared radar system.

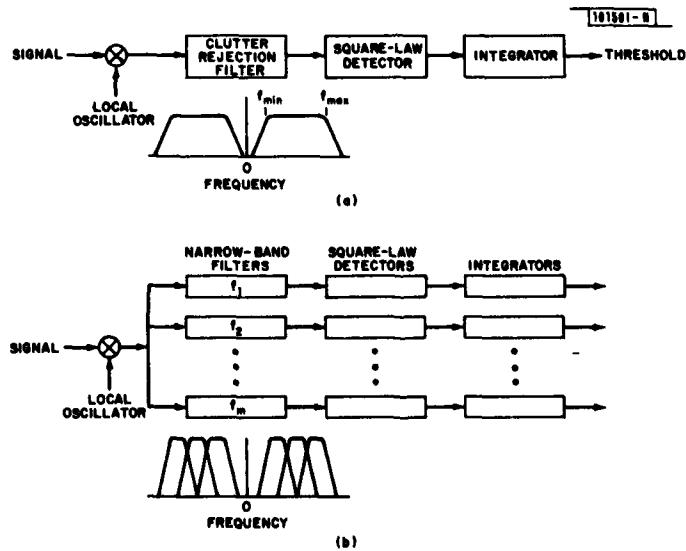


Fig. V-2. Signal processing required for: (a) clutter rejection, (b) noise rejection.

loss over a 3-km path to target (total of 18 dB) using a 10-W laser, and this should out perform visible-sensor and passive-infrared-sensor systems. Signal processors are often compared by their relative processing gains. Note that a 6-dB increase in processing gain provided by the SAW system would allow either an added 1 dB/km of bad weather penetration or a significant reduction in laser power.

### 3. Signal Processing Trade-offs

The purpose of the acquisition mode processor is to automatically, without operator intervention, determine if the return signal is reflected from a moving target. Clutter returns and noise are to be rejected. How slow a moving target can be reliably acquired depends on many different factors and is a question which will be determined experimentally. The goal is 1 mph (0.45 m/sec or 84 kHz).

Fig. V-2 is a diagram of the functional equivalent of the acquisition mode processor. As shown in Fig. V-2(a), the clutter rejection is accomplished by the equivalent of a highpass filter whose cutoff frequency  $f_{\min}$  is chosen so that the probability of false alarms  $P_{fa}$  generated by the clutter is within the system specification (e.g.,  $P_{fa} = 10^{-12}$ ). Noise at frequencies above the maximum Doppler shift  $f_{\max}$  is rejected by an appropriate filter.

• Actually the noise rejection is accomplished by a bank of filters as shown in Fig. V-2(b). Each filter in the band consists of a series combination of a bandpass filter of narrow width  $\Delta f$  which provides coherent integration for time  $\tau_c = 1/\Delta f$ , a square-law detector, and an integrator which provides noncoherent integration for time  $\tau_{nc}$ . Implementation of this kind of processor can take many forms, including chirp-transform spectrum analysis, which provides a serial rather than a parallel output.

The total integration time of the system should be made as long as possible. For the calculation presented below this was assumed to be 5 msec, as set by target size, scan rates, etc. With a 200- $\mu$ rad beam, and a scan rate of 1 rad/sec, this integration accumulates 25 pixels. The only free parameter in the noise rejection part of the system is the coherent integration time.

The system should penetrate as much bad weather with as small a laser source as possible. A reasonable system specification is for the signal-to-noise ratio to provide a probability of detection  $P_d = 0.95$ , with  $P_{fa} = 10^{-12}$ . What this signal-to-noise is, and more importantly, what laser power is required to achieve it, depends on the mix of coherent and noncoherent integration. In general, a fully coherent system has better performance (the relevant exception will be discussed below), and the extra amount of signal power required to achieve the same  $P_d$  and  $P_{fa}$  in the noncoherent system is called the integration loss. The integration loss (in dB), and equivalently the laser power required to achieve the same performance, is shown in Table V-1 for four systems with different mixes of coherent and noncoherent integration. The differences shown in Table V-1 are on the order of 5 dB. Whether such a difference is significant depends on the cost of alternative ways of obtaining gain, e.g., building a bigger laser, and upon the degree of knowledge one has concerning the system parameters and goals.

Coherent processing is generally superior to noncoherent processing. The relevant exception is integration of a signal which is fluctuating due to target scintillation or target speckle. If one makes the assumption that over the coherent integration interval the signal is constant and that successive intervals are uncorrelated, then a noncoherent processor will have better performance because it can average over the scintillations. If the speckle decorrelates in a

TABLE V-1  
MTI ACQUISITION SYSTEM TRADE-OFFS

	Trivial	Simple	Baseline	Super Resolution
Doppler Filter Bandwidth	10 MHz	1 MHz	100 kHz	10 kHz
Number of Filters/Detector	1	10	100	1000
Coherent Integration Time in Each Filter (μsec)	0.1	1	10	100
Number of Incoherent Integrations	50,000	5000	500	50
Relative Signal-Processing Loss (dB)	15.0	10.0	5.0	0
Laser Power Required (W)	100	32	10*	3.2

\* Nominal assumed power.

Assumptions:

Total dwell time on target = 5000 μsec

$$P_d = 0.95$$

$$P_{fa} = 10^{-12}$$

Maximum Doppler Shift = ±5 MHz (±60 mph)

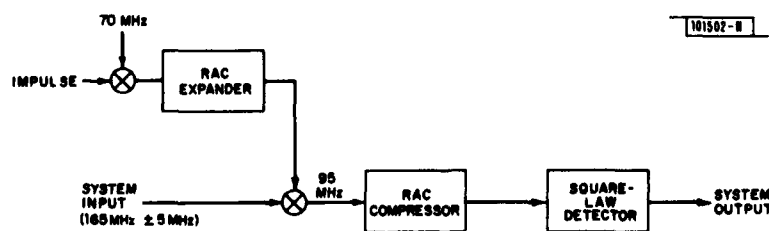


Fig. V-3. SAW chirp-transform processor.

distance on target comparable with the telescope diameter of 10 cm, the coherence time of the speckle should be on the order of 30  $\mu$ sec. This establishes an upper limit on the coherent integration time and provides for the averaging of 150 uncorrelated parts of the signal, thus overcoming any speckle loss.

The conclusions from the analysis are:

- (a) The baseline system (Doppler resolution of 100 kHz) offers enough performance advantage over a trivial or simple system to warrant its implementation.
- (b) The baseline system can also be used to measure target velocity to about 1 mph; thus additional equipment is not necessary for this secondary function.
- (c) The super-resolution system, while providing an additional 5 dB processing gain, imposes a severe constraint on laser spectral purity and mirror scan rates, and therefore should not be explored until the system and its operating environment are more fully characterized.

#### 4. Processor Implementation

A SAW chirp-transform system has been constructed and installed in the IRAR test van. A block diagram of the major elements of the signal processing equipment is shown in Fig. V-3. The important parameters are summarized in Table V-2. The operational principles of the processor are discussed elsewhere.<sup>3</sup>

The equipment was tested at the time of installation by using a signal derived from mixing the transmit laser with the local oscillator laser. (This mixing is part of the laser frequency-control-loop circuitry.) The laser spectrum was determined to have an instantaneous bandwidth (i.e., measured over 30  $\mu$ sec) which was smaller than the processor resolution of 33 kHz. Thus the spectral purity of the laser is well within the system requirements, and the SAW chirp-transform equipment was demonstrated to be completely compatible with the IRAR equipment.

J. T. Lynch      R. C. Williamson  
D. R. Arsenault   V. S. Dolat

TABLE V-2 SAW CHIRP-TRANSFORM PARAMETERS	
Dispersive Elements	Reflective Array Compressors (RACs) (WT products: 300, 1200)
Coherent Integration Time	30 $\mu$ sec (RAC dispersion)
Frequency Resolution	33 kHz
System Bandwidth	10 MHz
Duty Factor	50%
Side Lobes	unweighted, $\frac{\sin \omega T}{\omega T}$
Dynamic Range	$\approx 60$ dB

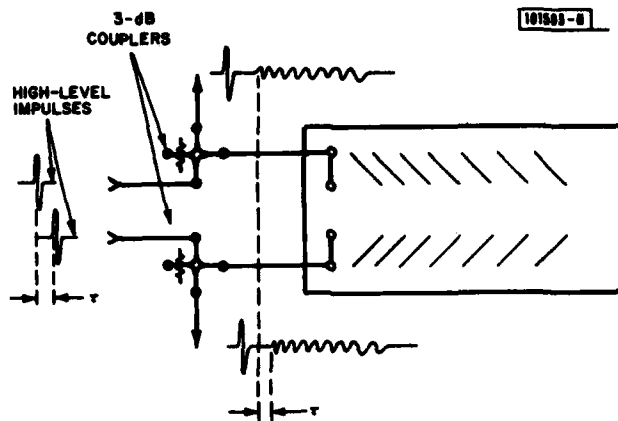


Fig. V-4. Sequential impulsing of a RAC device at both ports to obtain independent output chirp waveforms.

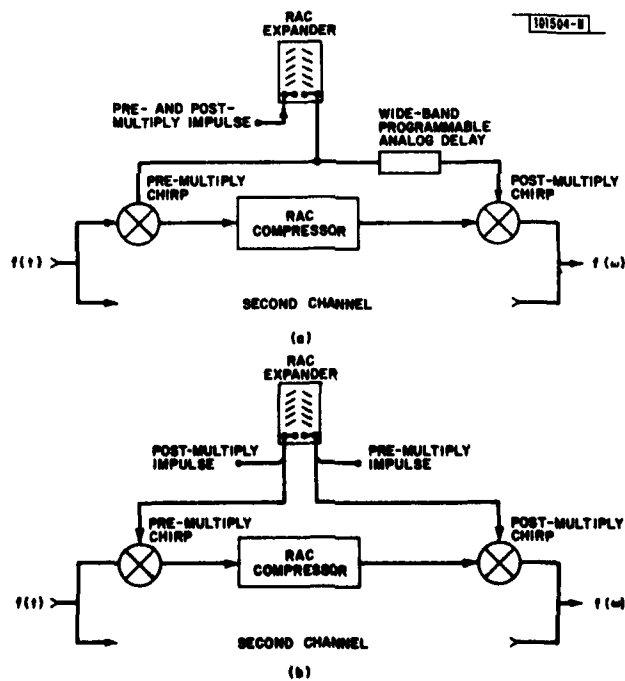


Fig. V-5. Schematic of one channel of chirp-transform system with: (a) singly impulsed RAC expander, which requires difficult-to-achieve programmable analog delay; (b) two-port impulsed RAC expander, which requires only programmable impulse timing.

## B. TWO-PORT IMPULSING OF RACs FOR HIGH-ACCURACY SAW TRANSFORM SYSTEMS

A novel solution to simplifying and maintaining accuracy in a chirp-Fourier-transform system is obtained by the process of sequentially impulsing each port of a reflective-array-compressor (RAC) device. This technique greatly simplifies the alignment procedures in such systems and reduces the total number of RACs required. In general, any passive linear time-invariant two-port device behaves identically whether one port or the other is used as the input, with the remaining port used as the output. Therefore, any SAW device possessing these properties can be utilized in the double-ended mode of operation shown schematically in Fig. V-4. Independent and identical output chirp waveforms separated by an interval  $\tau$  are obtained from opposite ports of the device simply by providing a differential delay  $\tau$  between the sequential impulses. Proper impulse timing and waveform gating is dependent on the system configuration.

One specific application where this technique is particularly useful is in a multiply-convolve-multiply implementation of the SAW chirp-Fourier-transform system,<sup>4</sup> which requires pre- and post-multiply chirp waveforms with very exacting delay characteristics to obtain high-accuracy transforms. Proper system alignment requires that the post-multiply waveform be delayed precisely with respect to the pre-multiply chirp. Difficulty is encountered in both the initial alignment and in the subsequent periodic recalibration which is required in order to compensate for temperature and aging variations of device characteristics. Improper timing affects three dominant system characteristics, namely, the time location of the input signal origin, the time location of the Fourier transform origin and the phase of the output used to discriminate between the real and imaginary Fourier components. In the original scheme, a portion of which is shown in Fig. V-5(a), the correct alignment would require a difficult realization of programmable delay in the RF signal path. The circuit diagrammed in Fig. V-5(b) provides an attractive method for generating the proper time delay required between the pre- and post-multiplying waveforms simply through use of digitally controlled timing of impulses applied to the RAC expander. The pedestal of delay normally introduced in RAC devices allows delay variations of several microseconds before overlap of the impulse with the generated chirp signal presents a problem.

Detailed system analysis has shown that a change in the pre-multiply chirp timing changes both the time position of the output Fourier transform and the phase of the output carrier, while a change in the post-multiply chirp timing shifts both the time origin of the input signal and the output phase. Thus, the input signal and Fourier transform origins can be conveniently and simply controlled by impulse timing. When impulse times are equally delayed, the phase of the output RF carrier remains constant, allowing separation of the real and imaginary Fourier components. If both impulses are not adjusted simultaneously and alike, there is a phase change in the output, but this is very easily compensated for by standard circuitry.

Spurious signals are introduced by the double impulsing, but these unwanted signals are weak. In a typical RAC device with simple input and output transducers, the double-transit signal through an expander with an insertion loss of 20 dB generates a spurious signal level which is approximately 20 dB below the expander waveform. However, since the double-transit wave has dispersion twice that of the desired waveform, it will suffer a further expansion loss of 3 dB in the compressor with no correlation gain. The double-transit signal will also experience increased conversion loss at the mixer. Hence, total spurious signal losses are estimated to be in the range where one can expect to maintain the full 40 dB of system dynamic range for noise-like input signals.



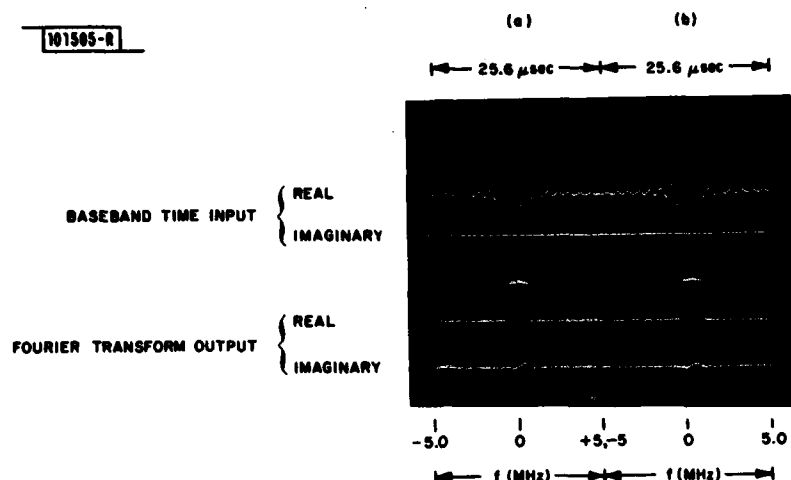


Fig. V-6. Input and output waveforms of chirp-transform system for (a) two-port impulsed RAC, (b) singly-impulsed RAC.

Figure V-6 shows the inputs and outputs of the two channels of a 100% chirp-transform system where the left-side output is evolved from a doubly-impulsed expander structure and the right-side output is evolved from the conventional singly-impulsed structure; the two compare favorably. In practice, the system will be periodically aligned by maintaining the output transforms of selected test tones through automatic adjustment of the impulse timing.

The details of using two-port impulsing of RAC devices to reduce the total device count for a 100% duty cycle transform system from four to only two are now being examined. Initial experiments have demonstrated the feasibility of this approach.

V. S. Dolat  
D. R. Arsenault

## C. DESIGN CRITERIA FOR SURFACE-ACOUSTIC-WAVE CONVOLVERS

### 1. Introduction

Recent developments in wideband surface-acoustic-wave (SAW) convolver configurations utilizing multistrip-coupler<sup>5</sup> and parabolic horn<sup>6</sup> beamwidth compression inevitably result in the surface wave energy being guided by a metal output electrode which is only a few wavelengths wide. Such guides are inherently dispersive<sup>5</sup> and lossy and will cause some degradation in convolver performance.

In the first part of this report it is shown that when electromagnetic effects are negligible<sup>7</sup> the effect of acoustic dispersion and attenuation can be represented by a linear time-invariant (LTI) filter in cascade with an ideal SAW convolver, and the appropriate formula for implementation loss (or degradation in signal-to-noise ratio relative to an ideal matched filter) is developed. In the second part, this formula is applied for two important modulation waveforms to calculate the implementation loss for some typical distortion filters equivalent to the overall effects of dispersion, attenuation, matching network, and transducer bandpass characteristics. The design criteria are presented in graphical form and provide useful guidelines with respect to acceptable tolerance on convolver phase, band shape, and band width.

## 2. LTI Filter Representation for Propagation Effects

For a convolver of length  $L$  in the propagation direction  $z$ , with the origin at the center, let the acoustic signals entering at each end be  $f(t)$  and  $g(t)$  having Fourier transforms  $F(f)$  and  $G(f)$ ; if  $\gamma(f) = \alpha(f) + j\beta(f)$  is the acoustic propagation constant, then the transforms of the two signals at position  $z$  are

$$F(f, z) = F(f) \exp\{-\gamma(L/2 + z)\} \quad \text{and} \quad G(f, z) = G(f) \exp\{-\gamma(L/2 - z)\} \quad (1)$$

The product of the corresponding time signals generated by the device nonlinearity produces a time-space-dependent open-circuit voltage having a Fourier transform  $V_{oc}(f, z)$  which is the convolution in the frequency domain

$$V_{oc}(f, z) = KF(f, z) * G(f, z) \quad (2)$$

where  $K$  is a nonlinearity constant. When  $L$  is electromagnetically short, the device open-circuit voltage is given by the integral of  $V_{oc}(f)$  from  $-L/2$  to  $+L/2$ . Using (1) and (2), the convolver open-circuit voltage is

$$V_{oc}(f) = K \int_{-\infty}^{\infty} P(f, \lambda) d\lambda \int_{-L/2}^{L/2} \exp\{-[\gamma(f - \lambda) - \gamma(\lambda)] z\} dz \quad (3)$$

where  $P(f, \lambda)$  is independent of  $z$ . Since for proper operation of the convolver as a matched filter the signal overlap must lie within the length  $L$ , the limits of the integral with respect to  $z$  can be set to infinity, and it can be shown that the integral with respect to  $z$  is the delta function  $v_g(f/2) \delta(f - 2\lambda)$ , where  $v_g(f/2)$  is the group velocity. Equation (3) hence simplifies to

$$V_{oc}(f) = KG(f/2) F(f/2) v_g(f/2) \exp\{-\gamma(f/2)\} \quad (4)$$

and one notes that the output frequency is at twice the input frequency. In an ideal nondispersive and lossless device

$$V_{oc}(f) = Kv_g F(f/2) G(f/2) \exp[-j\omega L/(2v_g)] \quad (5)$$

corresponding to a convolution in the time domain compressed by a factor of 2 with a delay  $L/v_g$ . Comparing (4) and (5), it can be seen that the output as given by (5) is equivalent to an ideal SAW convolver cascaded with an LTI distortion filter having a transfer function

$$D(f) = \exp[j\omega L/(2v_g) - \gamma(f/2) L] \quad (6)$$

where, for simplicity in the present discussion,  $v_g(f/2)$  in (4) has been equated to  $v_g$  and the effects of variations in  $v_g$  over the passband are included only in the  $\gamma$  part of the rapidly varying exponential term. Thus the effects of acoustic dispersion and attenuation are fully taken into account by cascading an ideal SAW convolver with the LTI filter  $D(f)$ . Including the transducer response  $T(f)$  and an output matching network  $H(f)$ , if  $S(f)$  and  $R(f)$  are the transforms of the electrical signal and reference waveforms, then the convolver output  $V_o(f)$  with distortion (omitting constant numerical factors) when operated as a matched filter with  $S = R^*$  is

$$V_o(f) = |S(f/2)|^2 T^2(f/2) D(f/2) H(f) = |S(f/2)|^2 Z(f) \quad (7)$$

where for compactness  $Z(f)$  is the convolver response function which lumps together all the departures from ideal; this is often called the convolver "F factor," and its magnitude and phase are routinely measured in the laboratory.

The implementation loss is thus given by

$$IL = \frac{\left| \int_{-\infty}^{\infty} |S(f)|^2 Z(f) df \right|^2}{\left( \int_{-\infty}^{\infty} |S(f)|^2 |Z(f)|^2 df \right) \left( \int_{-\infty}^{\infty} |S(f)|^2 df \right)} \quad (8)$$

Because all the integrations have infinite limits, the  $2 \times$  frequency expansion may be ignored, and in evaluating the integrals the various frequency functions can all be formulated in their baseband representation and a carrier frequency need not be specified. It is also clear in evaluating IL that the overall acoustic loss at the carrier frequency will cancel, so that in specifying  $Z(f)$  for implementation loss calculations only the frequency dependence of attenuation need be included in  $\gamma(f)$ .

### 3. Design Criteria

In a reasonably well designed device the convolver frequency response  $Z(f)$  is fairly flat in amplitude and its deviation from linear phase, although dominated by quadratic phase, often contains a small cubic phase contribution. The criteria presented here will essentially contrast the convolver implementation loss arising from phase distortion and amplitude-response shape for two important modulation waveforms: phase-shift-keyed (PSK) and minimum-shift-keyed (MSK).

Because the integrals in (8) have infinite limits, it is only the shapes of  $|S(f)|^2$  and  $Z(f)$  which are important; neither the carrier frequency nor the modulation chip rate need be specified, and implementation loss curves are obtained in terms of the following independent parameters: ratio  $R$  of convolver 3-dB bandwidth to chip rate, and quadratic phase, cubic phase, etc., at the convolver 3-dB band edges. The baseband functional forms of the spectral densities for PSK and MSK are used, and  $|Z(f)|$  is modeled by the cascade of two identical second-order Butterworth or Chebyshev responses since it is dominated by the product of two transducer responses. The Chebyshev response is designed to have a total ripple of 1 dB.

In Fig. V-7, the implementation loss for the Butterworth bandpass is shown plotted against the quadratic phase at the convolver 3-dB point for  $R = 0.6, 0.8$ , and  $1.0$ ; the solid curves are

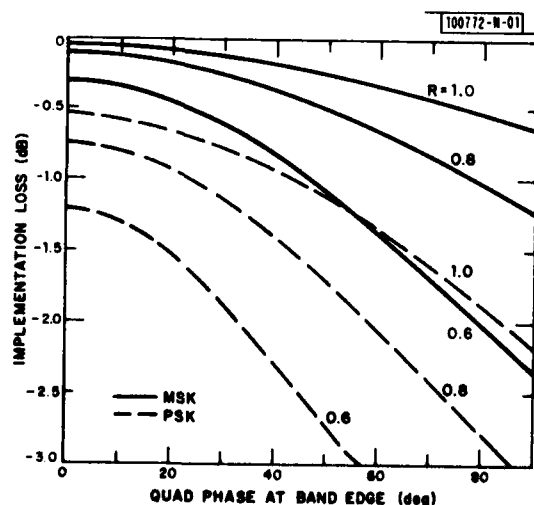
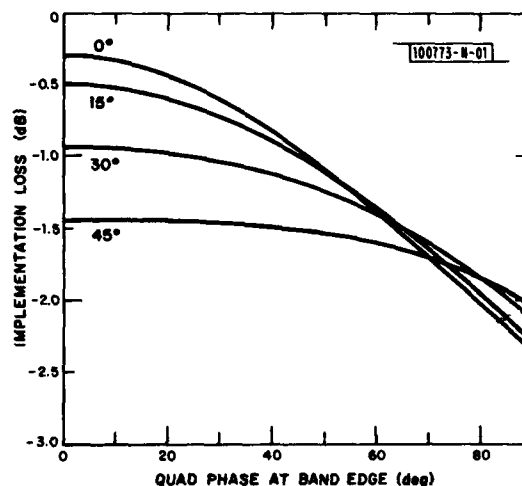


Fig. V-7. Implementation loss vs quadratic phase at the convolver 3-dB points for three ratios of convolver bandwidth to chip rate. MSK signal shown solid; PSK shown dashed.

for MSK modulation, the dashed curves for the PSK modulation. It can be seen that the MSK waveform is more spectrally efficient than the PSK in the sense that for a fixed chip rate and convolver bandwidth the implementation loss for MSK is less than that for PSK.

The curves given in Fig.V-7 summarize the various trade-offs between bandwidth, quadratic phase, and implementation loss. Similar results are obtained for a 1-dB-ripple Chebyshev bandpass; the implementation loss curves obtained for this case differ from Fig.V-7 by at most a few tenths of a dB and then only at extremely low values of quadratic phase.

Fig.V-8. Implementation loss vs quadratic phase at the convolver 3-dB points for four values of cubic phase at the convolver 3-dB points.



The effect of cubic phase on an MSK spectrum is shown in Fig.V-8 for a Butterworth bandpass with  $R = 0.6$ . Here it can be seen that cubic phase has a significant effect only when it is comparable with the quadratic phase. For a normalized bandwidth  $R = 1$ , the effect of up to  $45^\circ$  of cubic phase at the band edge is negligible.

In summary it has been shown that all the departures from an ideal convolver can be lumped into a single LTI transfer function  $Z(f)$ . Using this property, implementation loss predictions are given contrasting PSK and MSK waveforms in order to show property design trade-offs between convolver bandwidth, phase distortion, and implementation loss.

E. L. Adler<sup>†</sup>  
J. H. Cafarella  
J. H. Holtham

<sup>†</sup> Visiting scientist, McGill University, Montreal, P.Q.

#### REFERENCES

1. R.J. Hull and S. Marcus, "A Tactical 10.6  $\mu\text{m}$  Imaging Radar," Proceedings IEEE 1978 National Aerospace and Electronics Conference (IEEE, New York, 1978), pp.662-668.
2. R.J. Becherer, "System Design Study for Infrared Airborne Radar (IRAR)," Technical Note 1977-29, Lincoln Laboratory, M.I.T. (18 October 1977), DDC AD-A048979/9.
3. R.C. Williamson, "Wideband SAW Fourier-Transform Processor Design and Applications," Proc. IEE Intl. Specialist Seminar on Case Studies in Advanced Signal Processing, P.M. Grant, Ed., Peebles, Scotland, 18-21 September 1979, pp.237-243, Conf. Pub. No.180.
4. V.S. Dolat, M.B. Schulz, L.A. Veilleux, G.R. McCully, and R.C. Williamson, "High-Performance Hybrid SAW Chirp-Fourier-Transform System," in 1978 Ultrasonics Symposium Proceedings (IEEE, New York, 1978), pp.527-532, DDC AD-A069933/0.
5. Philippe Defranould and Charles Maerfeld, "A SAW Planar Piezoelectric Convolver," Proc. IEEE 64, 748-751, (1976).
6. R.A. Becker and D.H. Hurlburt, "Wideband  $\text{LiNbO}_3$  Elastic Convolvers with Parabolic Horns," in 1979 Ultrasonics Symposium Proceedings (IEEE, New York, 1979), pp.729-731.
7. D.P. Morgan and J.M. Hannah, "Effect of Electromagnetic Delays and SAW Dispersion in SAW Convolvers," in 1974 Ultrasonics Symposium Proceedings (IEEE, New York, 1974), pp.333-336.

UNCLASSIFIED

SECURITY CLASSIFICATION OF THIS PAGE (When Data Entered)

19 REPORT DOCUMENTATION PAGE		READ INSTRUCTIONS BEFORE COMPLETING FORM
1. REPORT NUMBER ESD TR-80-36	2. GOVT ACCESSION NO. AD-A092 724	3. RECIPIENT'S CATALOG NUMBER
4. TITLE (and Subtitle) Solid State Research, 1980:2 A089822		5. TYPE OF REPORT & PERIOD COVERED Quarterly Technical Summary 1 February - 30 April 1980
7. AUTHOR(s) Alan L. McWhorter		6. PERFORMING ORG. REPORT NUMBER 1980:2
9. PERFORMING ORGANIZATION NAME AND ADDRESS Lincoln Laboratory, M.I.T. P.O. Box 73 Lexington, MA 02173		8. CONTRACT OR GRANT NUMBER(s) F19628-80-C-0002
11. CONTROLLING OFFICE NAME AND ADDRESS Air Force Systems Command, USAF Andrews AFB Washington, DC 20331		10. PROGRAM ELEMENT, PROJECT, TASK AREA & WORK UNIT NUMBERS Program Element No. 63250F Project No. 649L
14. MONITORING AGENCY NAME & ADDRESS (if different from Controlling Office) Electronic Systems Division Hanscom AFB Bedford, MA 01731		12. REPORT DATE 15 May 1980
		13. NUMBER OF PAGES 68
		15. SECURITY CLASS. (of this report) Unclassified
		15a. DECLASSIFICATION DOWNGRADING SCHEDULE
16. DISTRIBUTION STATEMENT (of this Report)  Approved for public release; distribution unlimited.		
17. DISTRIBUTION STATEMENT (of the abstract entered in Block 20, if different from Report)		
18. SUPPLEMENTARY NOTES  None		
19. KEY WORDS (Continue on reverse side if necessary and identify by block number)		
solid state devices quantum electronics materials research microelectronics analog device technology	photodiode devices lasers laser spectroscopy imaging arrays signal processing	infrared imaging surface-wave transducers charge-coupled devices acoustoelectric devices
20. ABSTRACT (Continue on reverse side if necessary and identify by block number)  This report covers in detail the solid state research work of the Solid State Division at Lincoln Laboratory for the period 1 February through 30 April 1980. The topics covered are Solid State Device Research, Quantum Electronics, Materials Research, Microelectronics, and Analog Device Technology. Funding is primarily provided by the Air Force, with additional support provided by the Army, DARPA, Navy, NASA, NSF, and DOE.		

DD FORM 1 JAN 73 1473 EDITION OF 1 NOV 65 IS OBSOLETE

UNCLASSIFIED

SECURITY CLASSIFICATION OF THIS PAGE (When Data Entered)

207650

by